Journal of Power Sources 206 (2012) 129–143

Contents lists available at SciVerse ScienceDirect

Journal of Power Sources

journal homepage: www.elsevier.com/locate/jpowsour

A comprehensive yet comprehensible analytical model for the direct methanol fuel cell

Neal S. Rosenthal, Saurabh A. Vilekar, Ravindra Datta*

Fuel Cell Center, Department of Chemical Engineering, Worcester Polytechnic Institute, Worcester, MA 01609, United States

ARTICLE INFO

Article history:
Received 27 October 2011
Received in revised form 12 January 2012
Accepted 12 January 2012
Available online 24 January 2012

Keywords:
Direct methanol fuel cell (DMFC)
Methanol crossover
Oxygen crossover
DMFC model
DMFC polarization
DMFC efficiency

ABSTRACT

The direct methanol fuel cell (DMFC) has a significant potential in consumer electronics and in backup and portable power. Its progress is, however, hindered, in part, by a lack of an adequate fundamental understanding of the effect of various operating and design variables on its performance. While detailed computational models are available, an analytical model is attractive for ease of comprehension and ready utility. Therefore, we have developed a comprehensive yet tractable one-dimensional, isothermal, explicit analytical model based largely on *a priori* parameters, and in terms of quantities with tangible meaning.

The model correctly predicts the extent of methanol crossover and its effect on open-circuit voltage (OCV) as well as on polarization of the anode, cathode, and the fuel cell. It also accurately describes the effects of methanol feed concentration and temperature on DMFC performance. It aptly predicts the significant power losses from the large anode and cathode overpotentials as well as from methanol crossover, and the resulting low DMFC efficiency, except over a narrow range of operating conditions. The insightful model can be used, e.g., in real-time control of DMFC to operate in the narrow region of high efficiency and power density.

1. Introduction

The direct methanol fuel cell (DMFC) [1] is finding increasing application in portable, consumer electronics, and backup power. A key appeal of the DMFC is its ability to use a high energy density, commonly available, and an inexpensive liquid fuel, namely methanol. In comparison, hydrogen used by the conventional polymer-electrolyte membrane (PEM) fuel cell has distribution and storage challenges. The main shortcomings of the DMFC are low power density coupled with an order of magnitude larger amount of precious metal catalyst usage.

The conventional DFMC shares the polymer-electrolyte membrane as well as an intricate nanostructure with the PEM fuel cell [2]. Although great advances have been made in recent years in its design, operation, and performance, further progress depends in part on a better fundamental understanding of its functioning. Consequently, many theoretical models have been developed over the past decade, the majority belonging to two categories: (1) computational models [3], which involve few assumptions but provide only numerical results, and (2) semi-empirical models [4]. Both these approaches, naturally, provide limited insights. On the other hand, a tractable analytical model, developed from fundamental considerations coupled with appropriate simplifying assumptions, has the advantages of transparency and simplicity of usage. This is our objective here.

The key technological issues in DMFC are well known [1]. For one, methanol oxidation suffers from sluggish kinetics because the CO produced during the methanol oxidation reaction (MOR) blocks catalyst sites [5]. Another issue is that the membrane does not effectively keep the methanol and oxygen apart, because of its reliance on water for proton transport. Of course, where there is water, there is methanol. The resulting methanol crossover creates a mixed potential at the cathode and a low efficiency [6].

As a result, methanol feed concentration has a profound effect on the performance and efficiency of a DMFC; higher concentrations promoting CO poisoning of anode electrocatalyst and methanol crossover, but low concentrations providing low power densities [7–9]. Further, operating temperature can significantly influence electrode activation and Ohmic resistance [9] as well as methanol crossover [10]. PEM thickness increases Ohmic resistance, but

Abbreviations: ACL, anode catalyst layer; ADL, anode diffusion layer; CL, catalyst layer; CCL, cathode catalyst layer; CDL, cathode diffusion layer; DMFC, direct methanol fuel cell; ECSA, active electrocatalyst surface area; GDL, gas-diffusion layer; MEA, membrane electrode assembly; MOR, methanol oxidation reaction; OCV, open circuit voltage; OR, overall reaction; ORR, oxygen reduction reaction; PEM, polymer-electrolyte membrane; RDS, rate-determining step; TPI, three-phase interface.

* Corresponding author. Tel.: +1 508 831 6036.
E-mail address: rdatta@wpi.edu (R. Datta).

0378-7753/$ – see front matter © 2012 Elsevier B.V. All rights reserved.
doi:10.1016/j.jpowsour.2012.01.080

Nomenclature

A	MEA geometric area, cm^2
$c_{i,\alpha}$	concentration of species i in layer α, $mol\,cm^{-3}$
$c_{i,0}$	concentration of species i at equilibrium, $mol\,cm^{-3}$
$c_{i,b}$	concentration of species i in bulk phase, $mol\,cm^{-3}$
$c_{i,in}$	concentration of species i in feed, $mol\,cm^{-3}$
$c_{i,ref}$	reference concentration of species i, $mol\,cm^{-3}$
d	channel depth, cm
$d_{M,A}$	anode metal catalyst nanoparticle diameter, cm
$d_{M,C}$	anode metal catalyst nanoparticle diameter, cm
$D_{i,j}$	binary molecular diffusion coefficient between species i and j, $cm^2\,s^{-1}$
$D^e_{i,\alpha}$	effective diffusion coefficient of species i in layer α, $cm^2\,s^{-1}$
$D_{Me,A}$	diffusion of methanol in the anode gas diffusion layer
$D_{Me,W}$	diffusion of methanol in water
$D_{O,E}$	diffusion of oxygen in the cathode gas diffusion layer
$D_{O,W}$	diffusion of oxygen in water
E_{A,Φ_0}	anode effective activation energy for methanol oxidation reaction, $J\,mol^{-1}$
E_{C,Φ_0}	cathode effective activation energy for oxygen reduction reaction, $J\,mol^{-1}$
E_μ	activation energy for viscosity of water, $J\,mol^{-1}$
F	Faraday's constant, 96,487 C equiv.$^{-1}$
i	fuel cell current density ($A\,cm^{-2}$ of geometric electrode area)
$i_{A,0}$	anode exchange current density, $A\,cm^{-2}$
$i^*_{A,0,ref}$	anode reference exchange current density, anode, reference, $A\,cm^{-2}$ active metal catalyst area
$i_{A,L}$	anode limiting exchange current density, $A\,cm^{-2}$
$i_{C,0}$	cathode exchange current density, $A\,cm^{-2}$
$i^*_{C,0,ref}$	cathode reference exchange current density, $A\,cm^{-2}$ active metal catalyst area
$i_{C,L}$	cathode limiting exchange current density, $A\,cm^{-2}$
i_{X,O_2}	crossover current density of oxygen, $A\,cm^{-2}$
$i_{X,Me}$	crossover current density of methanol, $A\,cm^{-2}$
$i_{X,Me,L}$	limiting crossover current density of methanol, $A\,cm^{-2}$
i_ρ	electrode ρ current density, $A\,cm^{-2}$ geometric electrode area
i^*_ρ	current density, $A\,cm^{-2}$ metal catalyst surface
$i_{\rho,0}$	exchange current density, $A\,cm^{-2}$ geometric electrode area
$i^*_{\rho,0}$	exchange current density, $A\,cm^{-2}$ metal catalyst surface
K_{Me}	adsorption equilibrium constant
K_a	equilibrium constant for acid dissociation
k_i	bulk-phase mass transfer coefficient for species i, $cm\,s^{-1}$
k^*_ρ	rate constant for electrode reaction
k^*_{ρ,Φ_0}	rate constant corresponding to equilibrium electrode potential
L	channel length, cm
L_α	thickness of layer α, cm
$m_{M,A}$	anode catalyst loading, $g\,cm^{-2}$
$m_{M,C}$	cathode catalyst loading, $g\,cm^{-2}$
n	number of channels in parallel
$N_{i,z}$	flux of species i in the membrane along the z direction
$P_{i,\alpha}$	permeance of species i in layer α, $mol\,cm^{-1}$
$P^e_{i,\alpha}$	effective permeance of species i in layer α, including bulk-resistance, $mol\,cm^{-1}$
p_i	partial pressure of species i, atm
$p_{i,ref}$	reference partial pressure of species i, atm
q	heat dissipation flux, $W\,cm^{-2}$
q_{CO_2}	volume fraction of CO_2 bubbles inside ADL pore volume
q_W	volume fraction of water inside CDL pore volume
P	power density, $W\,cm^{-2}$
R	gas constant
Re	Reynolds number
R_I	interfacial resistance
r_ρ	reaction rate, $mol\,cm^{-2}$ geometric electrode area
r^*_ρ	reaction rate, $mol\,cm^{-2}$ metal catalyst surface
$r_{\rho,0}$	exchange reaction rate, $mol\,cm^{-2}$ geometric electrode area
$r^*_{\rho,0}$	exchange reaction rate, $mol\,cm^{-2}$ metal catalyst surface
Sc	Schmidt number
Sh	Sherwood number
T	temperature, K
T_{ref}	reference temperature, 298 K
V	cell voltage, V
V_0	thermodynamic voltage, V
V_{max}	maximum theoretical cell voltage determined from ΔH, V
$\dot{V}_A$	volumetric flow rate of anode feed, $cm^3\,s^{-1}$
$\dot{V}_C$	volumetric flow rate of cathode feed, $cm^3\,s^{-1}$
v	fluid velocity in flow channels, $cm\,s^{-1}$
x_i	mole fraction of species i
z_i	charge number of species i

Greek symbols

α	layer α
α_A	transfer coefficient, anode
α_C	transfer coefficient, cathode
$\dot{\alpha}_\rho$	transfer coefficient of the RDS in electrode reaction ρ
β	degree of acid dissociation in Nafion
$\gamma_{M,A}$	roughness factor, ratio of active anode catalyst surface area to MEA area
$\gamma_{M,C}$	roughness factor, ratio of active cathode catalyst surface area to MEA area
δ	ratio of mutual to matrix effective diffusion coefficients
ΔG	Gibbs free energy change $J\,mol^{-1}$
ΔH	enthalpy change $J\,mol^{-1}$
ε	fuel cell efficiency
ε_α	void fraction of layer α
η_A	anode overpotential, V
η_B	PEM overpotential, V
η_C	cathode overpotential, V
η_I	interfacial overpotential, V
η_ρ	overpotential of electrode reaction $\rho = \Phi - \Phi_{\rho,0}$, V
$\eta_{X,A}$	Anodic overpotential at cathode, V
$\eta_{X,C}$	Cathodic overpotential at anode, V
$\theta_{CO\cdot S}$	fraction of catalyst sites occupied by CO
$\theta_{CO\cdot S,ref}$	reference fraction of catalyst sites occupied by CO
$\kappa_{i,\alpha}$	partition coefficient of species i in layer α
λ	number of water molecules per sulfonic acid group in Nafion
$\nu_{\rho i}$	stoichiometric coefficient of species i in reaction ρ
$\nu_{\rho e^-}$	stoichiometric coefficient of electrons in reaction ρ

$\dot{\nu}_{\rho,e^-}$	stoichiometric coefficient of electrons in the RDS in electrode reaction ρ
ξ	electro-osmotic drag coefficient of water
$\rho_{M,A}$	anode catalyst metal density, g cm^{-3}
$\rho_{M,C}$	cathode catalyst metal density, g cm^{-3}
σ_B	effective PEM conductivity
τ_i	residence time of species i in electrode compartment, s
φ_I	fraction of metal surface in contact with ionomer
Φ	electrode potential, V
$\Phi_{\rho,0}$	half-cell thermodynamic (reversible) potential of electrode reaction ρ, V
Φ_C	Cathode potential, V
$\Phi_{A,0}$	Thermodynamic potential of anode, V
ω_{Ru}	mass fraction of Ru in anode catalyst

Subscripts/superscripts

·	rate-determining step
*	active metal catalyst area basis
0	equilibrium
A	anode layer
B	PEM layer
b	bulk-phase
C	cathode layer
D	anode diffusion layer
E	cathode diffusion layer
e^-	electron
I	interfacial or ionomer
i	species
in	feed
L	limiting
Me	methanol
ref	reference
W	water
X	crossover
α	layer in MEA
ρ	electrode (anode or cathode)

concomitantly reduces methanol crossover [11]. Finally, higher flow rates at anode and cathode can significantly reduce mass transfer limitations [12] and more effectively remove CO_2 and H_2O produced at the anode and cathode, respectively.

Over the past decade, there has been a significant advancement in the theoretical understanding of these issues. Only a handful of investigations are cited here for brevity. Thus, Sundmacher and Scott [13] developed a multilayer model for the membrane-electrode assembly (MEA), including unsteady-state mass balance, charge balance, diffusion, and electrode reaction kinetics, as well as thermodynamics of the two-phase CO_2–methanol–water gas–liquid mixture phase equilibria in the anode-diffusion layer (ADL). However, they neglected mass transfer limitations in the catalyst layer (CL) because of its thinness compared to the other layers. Garcia et al. [14] included the CL diffusion limitations in their semi-analytical solution approach. Their results indicate that the diffusion limitations are, in fact, generally small in the anode CL. Assuming Tafel kinetics, Kulikovsky [15] solved the ACL diffusion problem analytically, but only for asymptotically large and small currents.

Meyers and Newman [16] developed a detailed theoretical framework for describing non-ideal multicomponent transport in the various layers of the MEA, along with a multistep MOR, and used a finite-difference scheme to solve the coupled differential-algebraic equation system. However, the solution proved challenging because of multiple nonlinearities. Wang and Wang [17] devised a comprehensive two-phase multicomponent computational fluid dynamics (CFD) model capable of predicting the mixed potential effect at the cathode from methanol crossover, as well as the complete polarization plot. Chen and Zhao [18] developed a model for a passive DMFC to investigate the effects of heat and mass transport and electrochemical kinetics on overall performance. Rice and Faghri [19] investigated the one-dimensional mass transport of methanol vapor, water vapor, and carbon dioxide in a vapor-fed passive DMFC in order to numerically describe its temporal performance.

On the other hand, there are simpler, semi-empirical, algebraic models available in the literature, which are convenient for real-time simulation and control. Thus, Chiu et al. [4,20] have developed an algebraic semi-empirical model. Using the Levenberg–Marquardt algorithm, 8 model parameters were fitted based on regressing a set of 28 measurements. Using an additional 112-measurement data-set for model verification, they found that the proposed model was able to accurately predict methanol crossover as well as the DMFC performance and efficiency over a broad range of conditions. Dohle and Wippermann [21] developed a semi-empirical model describing the relationship between current and anode overpotential, cell potential versus current, and methanol permeation.

This paper provides an isothermal model of the DMFC that is based on a detailed consideration of the key transport and reaction processes, but uses defensible simplifying assumptions to obtain analytical solution. Thus, explicit analytical expressions are derived for the anode and cathode overpotentials in terms of current density, exchange current density, the limiting current density, and the crossover limiting current densities, in turn described in terms of basic mass transfer and kinetic parameters. Further, since oxygen can also, in principle, diffuse over to the anode in a DMFC [22], or can infiltrate from the CO_2 vent in a passive DMFC, the potential effect of any oxygen present at the cathode is also included. Additionally, power and heat generated in a DMFC is evaluated along with its efficiency. The model, involving a priori parameters, with the exception of two fitted parameters, is able to accurately predict the comprehensive set of experimental data of Chiu et al. [4,20] over a broad range of conditions.

2. Theory

2.1. Model description

Fig. 1 schematically shows the concentration profiles of methanol, oxygen, carbon dioxide, and water, as well as the anode and cathode potentials, Φ_A and Φ_C, across the various layers of the DMFC MEA.

Due to mass transfer limitations in the bulk phase of anode chamber as well as in the ADL, layer *D*, thus, the concentration of methanol drops as it is consumed via MOR in the anode catalyst layer (ACL), layer *A*, to produce CO_2, protons, and electrons. Furthermore, methanol concentration drops across the PEM, layer *B*, as methanol is transported across it via diffusion and electro-osmotic drag to arrive at the cathode, where it also undergoes MOR. The protons produced at the anode diffuse through the PEM to the cathode, whereas electrons commence their journey across the external circuit, arriving at the cathode, depleted from having performed external electrical work. Unlike as shown in the schematic, however, the methanol concentration actually declines somewhat within the ACL, as it is consumed in the MOR, and should properly be analyzed via a distributed diffusion-reaction model [14,15]. However, in order to obtain a simple analytical solution, it is assumed here to be uniform [13], based on considering the ACL

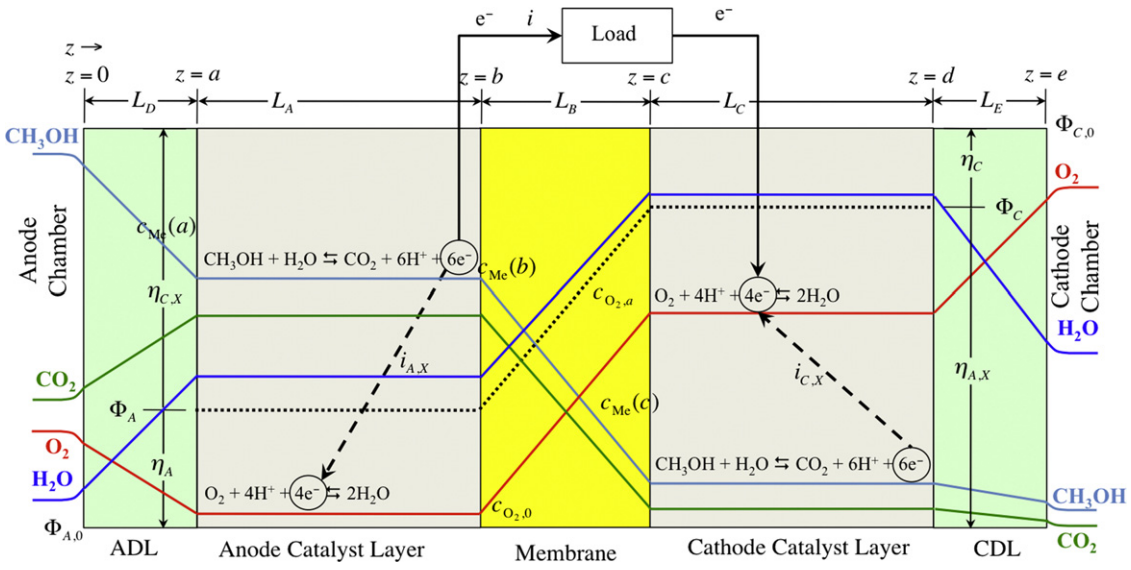

Fig. 1. Schematic representation of a DMFC MEA, including concentration profiles shown here for a concentrated methanol feed, external current and internal crossover currents, and potential profile across the various MEA layers.

as a thin layer, which is also tantamount to assuming a small Thiele modulus.

The MOR reaction, which is very sluggish owing to the strong CO catalyst adsorption at low temperatures, is facilitated by the anode overpotential, $\eta_A = \Phi_A - \Phi_{A,0}$, which in turn is determined by the drawn anode current density, i_A, comprising of both the external current i, as well as any current $i_{A,X}$, at the anode due to crossover/presence of O_2 in the anode chamber, i.e., $i_A = i + i_{A,X}$. The CO_2 that is produced at the anode can either diffuse/bubble across the ADL to be vented, or can, due to its high permeance [23], also diffuse across the PEM to be removed partly on the cathode side. Of course, a considerable amount of CO_2 is also produced at the cathode from methanol crossover.

Similarly, oxygen in the cathode chamber diffuses across the cathode diffusion layer (CDL), layer *E*, to arrive at the cathode catalyst layer (CCL), layer *C*, where it undergoes the oxygen reduction reaction (ORR) (Fig. 1). The ORR involves protons and electrons produced at the ACL and arriving via PEM and the external circuit, respectively. In addition, however, protons and electrons produced *in situ* at the CCL via MOR are utilized in the ORR. Thus, the cathode current density, $i_C = i + i_{C,X}$. The cathode overpotential, $\eta_C = \Phi_C - \Phi_{C,0}$, that is negative ($\eta_C < 0$), accelerates the ORR, which is otherwise exceedingly sluggish. The CCL is also considered as thin, i.e., without diffusion limitations, so that the concentrations within it are assumed to be uniform as well (Fig. 1).

The methanol arriving at the cathode also undergoes *electrochemical* MOR, rather than *chemical* oxidation, as sometimes believed [24], due to the huge overpotential there for the MOR, $\eta_{A,X} = \Phi_C - \Phi_{A,0}$ (Fig. 1), even when the external current $i = 0$, i.e., under open circuit voltage (OCV) conditions, effectively creating an internal short circuit, or a crossover current ($i_{C,X}$). In fact, since the thermodynamic voltage, $V_0 = \Phi_{C,0} - \Phi_{A,0}$ [2], we may alternately write $\eta_{A,X} = V_0 + \eta_C$, as shown in Fig. 1. As a result, we will assume below that the concentration of methanol in the CCL → 0. This assumption, as well as small concentration variations within the CL, is supported by the results of Garcia et al. [14]. Likewise, any oxygen, *albeit* to a much smaller extent, permeating from the cathode can also readily undergo electrochemical ORR due to large overpotential $\eta_{C,X} = \Phi_A - \Phi_{C,0}$, thus creating an internal crossover current ($i_{A,X}$).

2.2. Basic constitutive relations

In order to develop a simple *albeit* robust analytical model, and as is not uncommon, the electrode kinetics of the MOR and ORR, denoted generically as the electrode reaction ρ, are approximated here by the Butler–Volmer equation, though strictly this is valid only for the elementary steps involved in an overall electrode reaction [2], the overall electrode kinetics in reality being more nuanced [16,25]

$$\frac{i^*_\rho}{i^*_{\rho,0}} = \frac{i_\rho}{i_{\rho,0}} = \exp\left\{\frac{(\vec{\alpha}_\rho)\nu_{\rho e^-}F\eta_\rho}{RT}\right\} - \exp\left\{-\frac{(\bar{\alpha}_\rho)\nu_{\rho e^-}F\eta_\rho}{RT}\right\} \quad (1)$$

where $i^*_{\rho,0}$ (or $i_{\rho,0}$) is the exchange current density, $\nu_{\rho e^-}$ is the stoichiometric coefficient of electrons in the electrode reaction, and $\vec{\alpha}_\rho$ and $\bar{\alpha}_\rho$ are the fitted transfer coefficients of the forward and reverse electrode reaction. Here, the superscript asterisk denotes current density based on *actual* active electrocatalyst surface area (ECSA), while that without it denotes current density in terms of *geometric* MEA area.

Alternately, the transfer coefficients may be construed simply as the symmetry factor of the rate-determining step (RDS), typically taken as 1/2 for elementary reactions. In such an event, i.e., when it is justifiable to assume that $\vec{\alpha}_\rho = \bar{\alpha}_\rho \equiv \dot{\alpha}_\rho$, where the superscript dot implies RDS, the Butler–Volmer equation can be cast into the convenient form [2]

$$\frac{i^*_\rho}{i^*_{\rho,0}} = \left\{2\sinh\left(\frac{\dot{\alpha}_\rho \dot{\nu}_{\rho e^-}F\eta_\rho}{RT}\right)\right\} = \frac{r^*_\rho}{r^*_{\rho,0}} = \frac{k^*_\rho}{k^*_{\rho,\Phi_0}} \quad (2)$$

Here, the current density per unit MEA area, and kinetics of the electrode reaction are interrelated via [2]

$$i_\rho = \gamma_M i^*_\rho = \gamma_M(F\nu_{\rho e^-}r^*_\rho); \quad i_{\rho,0} = \gamma_M i^*_{\rho,0} = \gamma_M(F\nu_{\rho e^-}r^*_{\rho,0}) \quad (3)$$

as are the exchange current density and the corresponding rate. Here the roughness factor (γ_M) is the ratio between the active electrocatalyst area (ECSA) and the geometric area of the electrode/MEA. Further, the rate, r_ρ, defined on the basis of the geometric MEA area, $r_\rho = \gamma_M r^*_\rho$.

The electrode (both anode and cathode) reaction rate is further assumed to be pseudo first-order [2], along with the treatment of the electrode layer as an interface, i.e., a layer of small thickness,

so that the concentration of a species i within it is uniform (Fig. 1), e.g., for the anode, $c_{i,A} = c_{i,A}(a) = c_{i,A}(b)$, leading to

$$r^*_\rho = k^*_\rho c_{i,A}(a); \quad r^*_{\rho,0} = k^*_{\rho,\Phi_0} \kappa_{i,A} c_{i,b} \tag{4}$$

where $c_{i,b}$ is bulk-phase concentration of species i in the electrode chamber or flow channels, and $\kappa_{i,A}$ is the partition coefficient of the species i from the bulk-phase to the ACL, defined below.

More correctly, of course, $r^*_\rho = \varepsilon_\rho k^*_\rho c_i(a)$, in Eq. (4), where ε_ρ is the effectiveness factor, e.g., $\varepsilon_\rho = \tanh\phi_\rho/\phi_\rho$, where ϕ_ρ is the Thiele modulus for the electrode reaction, $\phi_\rho = L\sqrt{k^*_\rho/D^e_{i,\rho}}$, and L is the electrode layer thickness. However, numerical results [14] indicate that, for the relatively low current densities typically encountered in DFMCs, the assumption of unit effectiveness factor is acceptable, as implicit in Eq. (4) above.

For the one-dimensional (z-direction) flux (moles per unit area of the MEA) of a species i, the Nernst–Planck equation is used [26]

$$N_{i,z} = -D^e_i \left(\frac{dc_i}{dz} + z_i c_i \frac{F}{RT} \frac{d\phi}{dz} \right) + x_i N \tag{5}$$

where the terms in the parentheses represent diffusion and electromigration, respectively, while the last term represents convection. The electromigration term is, of course, zero for uncharged species ($z_i = 0$). Further, the relationship between flux of a species participating in the electrode reaction and the electrode current density is

$$i_\rho = N_{i,z} \left(\frac{\nu_{\rho e^-}}{-\nu_{\rho i}} F \right) \tag{6}$$

where, e.g., the stoichiometric coefficient of methanol in the MOR, $\nu_{A,\mathrm{Me}} = -1$.

The concentration of a species i in a layer α of the MEA in equilibrium with the bulk phase concentration is described in terms of the partition coefficient

$$\kappa_{i,\alpha} = \left(\frac{c_{i,\alpha}}{c_{i,b}} \right)_0 \tag{7}$$

which is, of course, a function of temperature and, for non-ideal mixtures, of concentration. Pseudo-equilibrium is assumed at the interface between two phases/layers. For instance, the partition coefficient of methanol [27] from bulk to the ADL, $\kappa_{\mathrm{Me},D}$, is determined in part by the fraction of the pore volume occupied by gas bubbles, and the vapor-liquid equilibrium [13]. In the absence of a gas phase within the ADL, it is approximately unity for a liquid feed, but not so for a vapor feed.

Across the bulk in the anode chamber as well as in the adjacent gas-diffusion layer (GDL), flux of a species i is constant at steady state, i.e.,

$$N_{i,D} = k_i \left\{ c_{i,b} - \frac{c_{i,D}(0)}{\kappa_{i,D}} \right\} = \frac{D^e_{i,D}}{L_D} \left\{ c_{i,D}(0) - c_{i,D}(a) \right\} \tag{8}$$

where the first equation represents the flux from the bulk phase (e.g., liquid or vapor phase methanol feed in the anode, or gas-phase O_2 in the cathode) to the GDL, while the second equation is the flux through the GDL. These two can be combined into the form

$$N_{i,D} = P^e_{i,D} \left\{ c_{i,b} - \frac{c_{i,D}(a)}{\kappa_{i,D}} \right\} \tag{9}$$

where $P^e_{i,D}$ is the effective (overall) permeance, or effective (overall) mass transfer coefficient, including both bulk mass transfer coefficient as well as GDL permeance, $P_{i,D}$

$$\frac{1}{P^e_{i,D}} \equiv \frac{1}{P_{i,D}} + \frac{1}{k_i}; \quad P_{i,D} \equiv \frac{\kappa_{i,D} D^e_{i,D}}{L_D} \tag{10}$$

A similar relation may be written for the cathode diffusion layer (CDL), layer E.

2.3. Methanol crossover and anode overpotential

Methanol that escapes reaction within the ACL can permeate readily through the PEM (layer B in Fig. 1) via diffusion and electro-osmotic drag

$$N_{\mathrm{Me},B} = \frac{D^e_{\mathrm{Me},B}}{L_B} \left\{ c_{\mathrm{Me},B}(b) - c_{\mathrm{Me},B}(c) \right\} + \frac{1}{c_{\mathrm{W},B} L_B} \left(\xi \frac{i}{F} \right) \int_0^{L_B} c_{\mathrm{Me},B} dz \tag{11}$$

represented, respectively, by the first and second terms on the right-hand side of this equation. This equation results from the integration of Eq. (5) for constant flux, in the absence of electromigration, and with the assumption that the methanol mole fraction within the PEM layer, $x_{\mathrm{Me},B} = c_{\mathrm{Me},B}/(c_{\mathrm{Me},B} + c_{\mathrm{W},B}) \approx c_{\mathrm{Me},B}/c_{\mathrm{W},B}$, because of the high molarity of water as compared to methanol. Here, ξ is the electro-osmotic drag coefficient, roughly 2.5 – 3.5 molecules of water per proton transported across the PEM [28].

As assumed above, the concentration within the ACL, $c_{\mathrm{Me},A} = c_{\mathrm{Me},A}(a) = c_{\mathrm{Me},A}(b)$, and further, that any methanol crossing over is consumed entirely within the CCL, i.e., $c_{\mathrm{Me},B}(c) \to 0$. These simplifications, along with the assumption of linear variation of methanol concentration within the electrolyte layer, B, reduce the membrane flux, Eq. (11), to

$$N_{\mathrm{Me},B} \approx \left(\frac{D^e_{\mathrm{Me},B}}{L_B} + \frac{i}{F} \frac{\xi}{2c_{\mathrm{W},B}} \right) \left(\frac{\kappa_{\mathrm{Me},B}}{\kappa_{\mathrm{Me},D}} \right) c_{\mathrm{Me},A}(a) \tag{12}$$

where it has been further assumed that the partition coefficient of methanol in the ACL is the same as that in the ADL, i.e., $\kappa_{\mathrm{Me},A} = \kappa_{\mathrm{Me},D}$.

Of course, using Eq. (6) with this, the crossover current due to the methanol flux across the PEM is

$$i_{X,\mathrm{Me}} = \left(\frac{\nu_{A,e^-}}{-\nu_{A,\mathrm{Me}}} \right) \left(\frac{D^e_{\mathrm{Me},B}}{L_B} F + i \frac{\xi}{2c_{\mathrm{W},B}} \right) \left(\frac{\kappa_{\mathrm{Me},B}}{\kappa_{\mathrm{Me},D}} \right) c_{\mathrm{Me},A}(a) \tag{13}$$

We will find it useful to define a *limiting* methanol crossover current density, i.e., the largest possible methanol diffusive flux across the PEM, which is under OCV conditions, i.e., when the external current, $i = 0$. Further, we imagine that under these conditions, there is little diffusion limitation across the ADL either, so that $c_{\mathrm{Me},A}(a) = c_{\mathrm{Me},D}(a) = c_{\mathrm{Me},D}(0) = \kappa_{\mathrm{Me},D} c_{\mathrm{Me},b}$ (Fig. 1), i.e., the methanol bulk concentration is available at the ACL-PEM interface. Thus, the corresponding limiting crossover current density of methanol, from Eq. (13), is

$$i_{X,\mathrm{Me},L} \equiv \left\{ \frac{D^e_{\mathrm{Me},B}}{L_B} \left(\frac{\nu_{A,e^-}}{-\nu_{A,\mathrm{Me}}} \right) F \right\} \kappa_{\mathrm{Me},B} c_{\mathrm{Me},b} \tag{14}$$

In reality, the crossover current at OCV (i.e., when $i = 0$) would be lower due to the finite methanol mass transfer resistance across the ADL, as discussed below. At any rate, using this *definition*, Eq. (13) is rewritten as

$$i_{X,\mathrm{Me}} = \left\{ \frac{i_{X,\mathrm{Me},L}}{\kappa_{\mathrm{Me},D} c_{\mathrm{Me},b}} + \left(\frac{\kappa_{\mathrm{Me},B}}{\kappa_{\mathrm{Me},D}} \right) \left(\frac{\nu_{A,e^-}}{-\nu_{A,\mathrm{Me}}} \right) i \frac{\xi}{2c_{\mathrm{W},B}} \right\} c_{\mathrm{Me},A}(a) \tag{15}$$

To determine this crossover current, thus, $c_{\mathrm{Me},A}(a)$ is needed. For this, we begin with a mass balance written around the ACL, assumed, as mentioned above, to be lumped, along with the use of Eq. (4), to provide

$$N_{\mathrm{Me},D}(a) - N_{\mathrm{Me},B}(b) = (-\nu_{A,\mathrm{Me}}) r_A = (-\nu_{A,\mathrm{Me}}) \gamma_M k^*_A c_{\mathrm{Me},A}(a) \tag{16}$$

This equation can be used to solve for $c_{\mathrm{Me},A}(a)$ by using in it Eqs. (9) and (12), along with $c_{\mathrm{Me},D}(a) = c_{\mathrm{Me},A}(a)$, since the partition coefficients in ADL and ACL have been assumed to be the same, i.e.,

$$c_{\mathrm{Me},A}(a) = \frac{\kappa_{\mathrm{Me},D} c_{\mathrm{Me},b}}{1 + \left\{ (D^e_{\mathrm{Me},B}/L_B) + (i/F)(\xi/2c_{\mathrm{W},B}) \right\} (\kappa_{\mathrm{Me},B}/P^e_{\mathrm{Me},D}) + (-\nu_{A,\mathrm{Me}})\gamma_M k^*_A \kappa_{\mathrm{Me},D}/P^e_{\mathrm{Me},D}} \tag{17}$$

where the last term in the denominator represents the ratio of the maximum rate of reaction within the ACL (when $c_{\mathrm{Me},A} = c_{\mathrm{Me},A}(a) = \kappa_{\mathrm{Me},D} c_{\mathrm{Me},b}$) to the maximum rate of diffusion through the ADL (when $c_{\mathrm{Me},A}(a) \to 0$), while the second term in the denominator represents methanol crossover.

Before returning to the crossover current, let us first use this expression in Eq. (3), along with Eq. (4), to provide the anode current density

$$i_A = \frac{\gamma_M F \nu_{A,\mathrm{e}^-} k^*_A \kappa_{\mathrm{Me},D} c_{\mathrm{Me},b}}{1 + \left\{ (D^e_{\mathrm{Me},B}/L_B) + (i/F)(\xi/2c_{\mathrm{W},B}) \right\} (\kappa_{\mathrm{Me},B}/P^e_{\mathrm{Me},D}) + (-\nu_{A,\mathrm{Me}})\gamma_M k^*_A \kappa_{\mathrm{Me},D}/P^e_{\mathrm{Me},D}} \tag{18}$$

When the rate of diffusion in the ADL is significantly less than the rate of the overall electrode reaction, the "1" may be neglected compared to the other terms in the denominator. Of course, then the crossover term is also negligible, as then $c_{\mathrm{Me},D}(a) \to 0$. This, therefore, *defines* the ADL diffusion-restricted anode limiting current density from above, i.e.,

$$i_{A,L} \equiv \left(\frac{\nu_{A,\mathrm{e}^-}}{-\nu_{A,\mathrm{Me}}} \right) F P^e_{\mathrm{Me},D} c_{\mathrm{Me},b} \tag{19}$$

corresponding to the maximum possible diffusion flux across the ADL.

The previous two equations can be combined and rewritten as a ratio between the anode current density and its diffusion-restricted limiting current density

$$\frac{i_A}{i_{A,L}} = \frac{(-\nu_{A,\mathrm{Me}})\gamma_M k^*_A \kappa_{\mathrm{Me},D}/P^e_{\mathrm{Me},D}}{1 + \left\{ (D^e_{\mathrm{Me},B}/L_B) + (i/F)(\xi/2c_{\mathrm{W},B}) \right\} (\kappa_{\mathrm{Me},B}/P^e_{\mathrm{Me},D}) + (-\nu_{A,\mathrm{Me}})\gamma_M k^*_A \kappa_{\mathrm{Me},D}/P^e_{\mathrm{Me},D}} \tag{20}$$

which can be further rearranged as

$$\frac{(-\nu_{A,\mathrm{Me}})\gamma_M k^*_A \kappa_{\mathrm{Me},D}}{P^e_{\mathrm{Me},D}} = \left(\frac{i_A/i_{A,L}}{1 - i_A/i_{A,L}} \right) \left[1 + \left\{ \frac{D^e_{\mathrm{Me},B}}{L_B} + \frac{i}{2F} \frac{\xi}{c_{\mathrm{W},B}} \right\} \frac{\kappa_{\mathrm{Me},B}}{P^e_{\mathrm{Me},D}} \right] \tag{21}$$

Using Eqs. (14) and (19) for the term within the square brackets on the right-hand side of this equation, it may be recast as

$$\frac{(-\nu_{A,\mathrm{Me}})\gamma_M k^*_A \kappa_{\mathrm{Me},D}}{P^e_{\mathrm{Me},D}} = \left(\frac{i_A/i_{A,L}}{1 - i_A/i_{A,L}} \right) \times \left[1 + \frac{1}{i_{A,L}} \left\{ i_{X,\mathrm{Me},L} + \left(\frac{\nu_{A,\mathrm{e}^-}}{-\nu_{A,\mathrm{Me}}} \right) \frac{\kappa_{\mathrm{Me},B}}{\kappa_{\mathrm{W},B}} \frac{x_{\mathrm{Me},b}}{2} \xi(i) \right\} \right] \tag{22}$$

where the ratio of concentrations, $c_{\mathrm{Me},b}/c_{\mathrm{W},B} = (c_{\mathrm{Me},b}/c_{\mathrm{W},b})(c_{\mathrm{W},b}/c_{\mathrm{W},B}) \approx x_{\mathrm{Me},b}/\kappa_{\mathrm{W},B}$, where $x_{\mathrm{Me},b}$ is the mole fraction of methanol in the bulk and $\kappa_{\mathrm{W},B}$ is the partition coefficient of water in the membrane, i.e., $\kappa_{\mathrm{W},B} \equiv c_{\mathrm{W},B}/c_{\mathrm{W},b}$

Also, from Eqs. (3), (4) and (19), we can write ratio of the anode exchange-current density to its diffusion-restricted limiting current density as

$$\frac{i_{A,0}}{i_{A,L}} = \frac{(-\nu_{A,\mathrm{Me}})\gamma_M k^*_{A,\Phi_0} \kappa_{\mathrm{Me},D}}{P^e_{\mathrm{Me},D}} \tag{23}$$

Combining the last two equations, thus, the ratio of anode rate constant to that at equilibrium anode potential

$$\frac{k^*_A}{k^*_{A,\Phi_0}} = \left(\frac{i_A/i_{A,0}}{1 - i_A/i_{A,L}} \right) \times \left[1 + \frac{1}{i_{A,L}} \left\{ i_{X,\mathrm{Me},L} + \left(\frac{\nu_{A,\mathrm{e}^-}}{-\nu_{A,\mathrm{Me}}} \right) \frac{\kappa_{\mathrm{Me},B}}{\kappa_{\mathrm{W},B}} \frac{x_{\mathrm{Me},b}}{2} \xi(i) \right\} \right] \tag{24}$$

Finally, combining this with Eq. (2) provides

$$2 \sinh \left(\frac{\dot{\alpha}_A \dot{\nu}_{A,\mathrm{e}^-} F \eta_A}{RT} \right) = \left(\frac{i_A/i_{A,0}}{1 - i_A/i_{A,L}} \right) \times \left[1 + \frac{1}{i_{A,L}} \left\{ i_{X,\mathrm{Me},L} + \left(\frac{\nu_{A,\mathrm{e}^-}}{-\nu_{A,\mathrm{Me}}} \right) \frac{\kappa_{\mathrm{Me},B}}{\kappa_{\mathrm{W},B}} \frac{x_{\mathrm{Me},b}}{2} \xi(i) \right\} \right] \tag{25}$$

which may be further inverted to provide an explicit equation for the anode overpotential

$$\eta_A = \frac{RT}{\dot{\alpha}_A \dot{\nu}_{A,\mathrm{e}^-} F} \sinh^{-1} \left[\left\{ \frac{1}{2} \left(\frac{i_A/i_{A,0}}{1 - i_A/i_{A,L}} \right) \right\} \left\{ i_{X,\mathrm{Me},L} + 3 \left(\frac{\kappa_{\mathrm{Me},B}}{\kappa_{\mathrm{W},B}} \right) x_{\mathrm{Me},b} \xi(i) \right\} \right] \tag{26}$$

being the combined overpotential associated with kinetic and diffusional processes, both in the bulk and in the GDL, as well as the effect of methanol crossover on it. In the above, we have used $\nu_{A,\mathrm{e}^-}/(-\nu_{A,\mathrm{Me}}) = +6/\{-(-1)\} = +6$ for the MOR.

Returning now to the issue of methanol crossover current, using Eqs. (14), (17) and (22) in Eq. (15),

$$i_{X,\mathrm{Me}} = \frac{\left\{ i_{X,\mathrm{Me},L} + 3(\kappa_{\mathrm{Me},B}/\kappa_{\mathrm{W},B}) x_{\mathrm{Me},b} \xi(i) \right\} (1 - i/i_{A,L})}{[1 + (1/i_{A,L}) \left\{ i_{X,\mathrm{Me},L} + 3(\kappa_{\mathrm{Me},B}/\kappa_{\mathrm{W},B}) x_{\mathrm{Me},b} \xi(i) \right\}]} \tag{27}$$

where again $\nu_{A,\mathrm{e}^-}/(-\nu_{A,\mathrm{Me}}) = 6$ for MOR has been used, and we have further assumed in the last term in the numerator that the anode current, $i_A = i + i_{X,\mathrm{O}_2} \approx i$, i.e., $i_{X,\mathrm{O}_2} \to 0$.

Finally, under OCV conditions ($i = 0$), this reduces down to

$$i_{X,\mathrm{Me},0} = \frac{i_{X,\mathrm{Me},L}}{1 + (i_{X,\mathrm{Me},L}/i_{A,L})} \tag{28}$$

which, as alluded to above, suitably tempers the limiting crossover current density defined by Eq. (14) by the diffusion limitations within the ADL under OCV conditions.

2.4. DMFC polarization

The observed voltage in a DMFC is determined by the difference between the thermodynamic voltage and the anodic overpotential, the cathodic overpotential, the Ohmic losses in the PEM, as well as any internal resistance exhibited by the PEM [2,22], i.e.,

$$V = V_0 - \eta_A + \eta_C + \eta_B - \eta_I \tag{29}$$

where the anode polarization, with the anode current, $i_A = i + i_{X,\mathrm{O}_2}$, in Eq. (26) is

$$\eta_A = \frac{RT}{\dot{\alpha}_A \dot{\nu}_{A,\mathrm{e}^-} F} \sinh^{-1} \left[\frac{1}{2} \left\{ \frac{(i + i_{X,\mathrm{O}_2})/i_{A,0}}{1 - (i + i_{X,\mathrm{O}_2})/i_{A,L}} \right\} \times \left\{ 1 + \frac{1}{i_{A,L}} \left(i_{X,\mathrm{Me},L} + 3 \left(\frac{\kappa_{\mathrm{Me},B}}{\kappa_{\mathrm{W},B}} \right) x_{\mathrm{Me},b} \xi i \right) \right\} \right] \tag{30}$$

i.e., the anode overpotential is affected by *both* methanol crossover as well as oxygen crossover or alternate infiltration into the anode chamber. This effect of the presence of oxygen at the anode on its polarization has not so far been discussed in the literature. Neither has the effect of methanol crossover on *anode* overpotential.

In a manner similar to that described in the last sub-section for anode, the cathode polarization may also be determined, providing

$$\eta_C = \frac{RT}{\dot{\alpha}_C \dot{\nu}_{C,e^-} F} \sinh^{-1}\left\{\frac{1}{2}\left(\frac{(i+i_{X,Me})/i_{C,0}}{1-(i+i_{X,Me})/i_{C,L}}\right)\right\} \tag{31}$$

where it is assumed that the effect of the crossover of oxygen through the membrane on *cathode* polarization is small, i.e., it can be treated virtually as impervious [2,22], so that the cathode overpotential is affected by only methanol crossover. Further, $\eta_C < 0$ here, of course, because $\nu_{C,e^-} < 0$ [2].

The CDL diffusion restricted cathode limiting current density, in analogy to Eq. (19) is

$$i_{C,L} \equiv 4FP^e_{O_2,E} c_{O_2,b} \tag{32}$$

while the effective permeance of oxygen in the CDL is given by Eq. (10), i.e.,

$$P^e_{O_2,E} = \left(\frac{L_E}{\kappa_{O_2} D^e_{O_2,E}} + \frac{1}{k_{O_2}}\right)^{-1} \tag{33}$$

The oxygen crossover current may be roughly estimated as follows. There are, in fact, two sources of oxygen: (1) in anode methanol feed itself, assuming it is saturated with oxygen from the air, and (2) from the cathode air feed. Assuming that the anode oxygen at the ACL is limited by the diffusion across the ADL, Eq. (19) can be adopted for it, while the cathode oxygen is limited by diffusion across the CDL as well as the PEM layer, which can be approximated using Eq. (28). Thus, assuming

$$\begin{aligned} i_{X,O_2} &= \left\{P_{O_2,D} + \left(\frac{1}{P^e_{O_2,E}} + \frac{1}{P_{O_2,B}}\right)^{-1}\right\} 4Fc_{O_2,b} \\ &\approx (P_{O_2,D} + P_{O_2,B}) 4Fc_{O_2,b} \end{aligned} \tag{34}$$

where the simplification indicated in the second equality in Eq. (32) results because the permeance of O_2 in CDL is much larger than the permeance of O_2 in the PEM. This is because while the diffusion in the CDL is mostly in the gas phase, that in the ADL is mainly in the liquid phase.

In the above, the oxygen permeance in PEM

$$P_{O_2,B} \equiv \frac{\kappa_{O_2} D^e_{O_2,B}}{L_B} \tag{35}$$

while the effective permeance of oxygen in the ADL is given by Eq. (10).

Finally, the combination of Eqs. (29), (30) and (31) provides the DMFC polarization

$$\begin{aligned} V = V_0 &- \frac{RT}{\dot{\alpha}_A \dot{\nu}_{A,e^-} F} \sinh^{-1}\left[\frac{1}{2}\left\{\frac{(i+i_{X,O_2})/i_{A,0}}{1-(i+i_{X,O_2})/i_{A,L}}\right\}\right. \\ &\left.\times\left\{1+\frac{1}{i_{A,L}}\left(i_{X,Me,L}+3\left(\frac{\kappa_{Me,B}}{\kappa_{W,B}}\right)x_{Me,b}\xi i\right)\right\}\right] \\ &+ \frac{RT}{\dot{\alpha}_C \dot{\nu}_{C,e^-} F} \sinh^{-1}\left\{\frac{1}{2}\left(\frac{(i+i_{X,Me})/i_{C,0}}{1-(i+i_{X,Me})/i_{C,L}}\right)\right\} \\ &- \frac{iL_B}{\sigma_B} - i(R_I) \end{aligned} \tag{36}$$

where the second-to-last term on the right-hand side is the Ohmic overpotential in the electrolyte layer, and R_I is any interfacial MEA resistance due to imperfect bonding of different layers or due to partial delamination with use.

Finally, the power density (W cm^{-2} MEA) produced by the DMFC can be obtained simply from $P = iV$, i.e.,

$$\begin{aligned} P = iV_0 &- \frac{iRT}{\dot{\alpha}_A \dot{\nu}_{A,e^-} F} \sinh^{-1}\left[\frac{1}{2}\left\{\frac{(i+i_{X,O_2})/i_{A,0}}{1-(i+i_{X,O_2})/i_{A,L}}\right\}\right. \\ &\left.\times\left\{1+\frac{1}{i_{A,L}}\left(i_{X,Me,L}+3\left(\frac{\kappa_{Me,B}}{\kappa_{W,B}}\right)x_{Me,b}\xi i\right)\right\}\right] \\ &+ \frac{iRT}{\dot{\alpha}_C \dot{\nu}_{C,e^-} F} \sinh^{-1}\left\{\frac{1}{2}\left(\frac{(i+i_{X,Me})/i_{C,0}}{1-(i+i_{X,Me})/i_{C,L}}\right)\right\} \\ &- \frac{i^2 L_B}{\sigma_B} - i^2(R_I) \end{aligned} \tag{37}$$

This completes the development of our analytical model for the DMFC. It is seen that it is quite tractable and that many of the terms in the equations have tangible meaning.

2.5. Model parameters

The veracity of above-developed analytical model and its underlying assumptions is ascertained by comparing it to experimental data, using the best available model parameters in the literature, with a minimal of fitted parameters.

The thermodynamic DMFC cell potential in Eq. (36) is given by

$$V_0 = 1.214 - 1.4\times10^{-4}(T-298) + \frac{RT}{6F}\ln\left\{\frac{a_{Me}}{a_{H_2O}}\left(\frac{p^{3/2}_{O_2}}{p_{CO_2}}\right)\right\} \tag{38}$$

where the first term on the right-hand side represents the *standard* DMFC cell voltage, $V^o_0 = 1.214$ V, corrected for temperature and species activities by the remaining two, with partial pressures given in bars or in atmospheres. We assume the activity of water to be unity, and replace the activity of methanol by its mole fraction for dilute feeds. Then, under the usual DMFC operating conditions, the thermodynamic DMFC cell potential $V_0 \approx 1.18$ V.

Let us next consider electrode kinetics. Both the MOR [29] and the ORR [30] are very complex electrode reactions with multiple steps and pathways. There is no definitive word yet in the literature on the mechanism or kinetics of either of these important reactions. In fact, even an unequivocal value for the exchange current density of MOR is not yet available.

For the ORR, as usual, we assume the Butler–Volmer form of Eq. (2) along with $\dot{\alpha}_C = 1/2$ and $\dot{\nu}_{C,e^-} = -2$, construed as those corresponding to the RDS, where the exchange current density is given by [22]

$$i_{C,0} = \gamma_{M,C}\left(\frac{c_{O_2,0}}{c_{O_2,ref}}\right)\exp\left[-\frac{E_{C,\Phi_0}}{R}\left(\frac{1}{T}-\frac{1}{T_{ref}}\right)\right] i^*_{C,0,ref} \tag{39}$$

where $c_{O_2,0}$ is the concentration in the CCL under equilibrium conditions, i.e., $c_{O_2,0} = \kappa_{O_2,C} c_{O_2,b}$, also accounting for the water vapor pressure, along with the reference exchange current density $i^*_{C,0,ref} = 1.0\times10^{-10}$ A cm^{-2} at $T_{ref} = 298$ K, reference concentration corresponding to $p_{O_2,ref} = 1.0$ atm, and an effective activation energy $E_{C,\Phi_0} = 67,000$ J mol^{-1} [22].

Here, the relationship between the actual rates of electrodic reactions on the basis of unit triple-phase interface (TPI) area, and those observed experimentally on the basis of unit geometric MEA area is governed by the electrocatalyst surface roughness, which may be estimated from [2]

$$\gamma_M = \varphi_I m_M \frac{6}{\rho_M d_M} \tag{40}$$

where ρ_M is the catalyst density, m_M is the catalyst leading, d_M is the supported or unsupported catalyst crystallite diameter, and

φ_l is the fraction of metal catalyst surface in contact with the ionomer, forming the TPI. It may be noted that for Pt–Ru alloy, $\rho_{M,A} = (1-\omega_{Ru})\rho_{Pt} + \omega_{Ru}\rho_{Ru}$ where ω_{Ru} is the mass fraction of Ru, $\rho_{Pt} = 21.4\,g\,cm^{-3}$, $\rho_{Ru} = 12.3\,g\,cm^{-3}$.

For the case of the MOR on the conventional Pt–Ru anode, the dual site mechanism is broadly accepted [31], wherein the methanol adsorbs and dissociates into adsorbed carbon monoxide, CO · Pt, on Pt sites [32], covering these almost completely at lower temperatures and overpotentials because of its strong adsorption, while water dissociates more readily on the Ru sites into adsorbed OH, i.e., OH · Ru, which finally oxidizes the adsorbed CO into CO_2, releasing the Pt sites on which the electrochemical MOR can then be repeated, starting with the adsorption of methanol, and then proceeding through step-wise dehydrogenation to produce CO · Pt.

Assuming then the first step in the MOR sequence, $CH_3OH + Pt \rightleftarrows CH_3OH \cdot Pt$, to be the RDS in the sequence [5], we may write the rate of the electrode reaction as $\vec{r}_1 \approx \vec{k}_1 c_{Me}(1-\theta_{CO\cdot S})$, in which $\theta_{CO\cdot S}$ represents the catalyst site fraction occupied by carbon monoxide, the site fractions of other adsorbed species (H · S and CH_3OH · S, etc.) being considered negligible. Thus, the Butler–Volmer form of Eq. (2), along with $\dot{\alpha}_A = 1/2$, and $\dot{\nu}_{A,e^-} = +1$ [33], is assumed to describe the potential dependence, where the exchange current density is given by

$$i_{A,0} = \gamma_{M,A}\frac{c_{Me,0}}{c_{Me,ref}}\left(\frac{1-\theta_{CO\cdot S}}{1-\theta_{CO\cdot S,ref}}\right) \times \exp\left[-\frac{E_{A,\Phi_0}}{R}\left(\frac{1}{T}-\frac{1}{T_{ref}}\right)\right] i^*_{A,0,ref} \quad (41)$$

where $c_{Me,0}$ is the ACL concentration under equilibrium conditions, i.e., $c_{Me,0} = \kappa_{Me,A}c_{Me,b}$, the reference methanol concentration, $c_{Me,ref} = 1.0\times10^{-3}\,mol\,cm^{-3}$, and the MOR activation energy, $E_{A,\Phi_0} = 65,000\,J\,mol^{-1}$ [34], reported for Pt–Ru catalyst particles in contact with Nafion electrolyte [34]. This is close to the value of $60{,}000\,J\,mol^{-1}$ determined by Gasteiger et al. [35] for liquid electrolyte, and is further consistent with first-principles calculations [36]. In comparison, Gojkovic et al. [33] provide an activation energy of about $70\,kJ\,mol^{-1}$.

The fraction of sites covered by CO, $\theta_{CO\cdot S}$, in the exchange-current density expression is assumed to be given by the Langmuir isotherm

$$\theta_{CO\cdot S} = \frac{K_{Me}c_{Me,0}}{1+K_{Me}c_{Me,0}} \quad (42)$$

where the adsorption equilibrium constant is assumed to be that for CO adsorption on Pt [32]

$$K_{Me} = 1.41\times10^{-8}\,\exp\left(\frac{130,000\,J\,mol^{-1}}{RT}\right) \quad (43)$$

For the Pt–Ru anode, we have assumed a reference intrinsic exchange current density for MOR as $i^*_{A,0,ref} = 2\times10^{-8}\,A\,cm^{-2}$. This is one of the two main fitted parameters in our model. Although exchange current densities for MOR have been reported in the literature for anode, they often include the catalyst surface roughness, not usually reported. In other words, a definitive value for $i^*_{A,0,ref}$ has not so far been reported.

It is evident from this that even on state-of-the art Pt–Ru catalyst, the MOR is an exceedingly slow reaction, much as ORR is, and is a key reason for the rather lackluster performance of DMFCs, and a requirement for high catalyst loading. This further means that, because of the low methanol conversion in the ACL despite the high catalyst loadings, much of it is left over for diffusion across PEM to the cathode, further impacting the cathode polarization and also reducing the current efficiency.

Next, let us consider the various transport parameters. The methanol–water binary diffusion coefficient at infinite dilution is fitted to the available experimental data [37] as

$$D_{Me,W} = 2.1\times10^{-5}\,\exp\left\{-\frac{20,460}{R}\left(\frac{1}{T}-\frac{1}{313}\right)\right\}\,cm^2\,s^{-1} \quad (44)$$

The effective diffusion coefficient of species i in a layer α, $D^e_{i,\alpha}$, is dependent on the volume fraction ε of the diffusing phase in the layer α [2,13], i.e., $D^e_{i,\alpha} = \varepsilon^{1.5}D_{i,\alpha}$, where $D_{i,\alpha}$ is the molecular diffusion coefficient in phase α, available from experiments or predicted from theory (as in gaseous mixture), and the exponent 1.5 is the so-called Bruggeman exponent of volume fraction ε, accounting for both the porosity and the tortuosity factor [38].

To simulate the effect of carbon dioxide and water buildup within the ADL and CDL, respectively, on the effective diffusion coefficients, thus, corresponding volume fraction terms ought to be included. For instance, since the transport of oxygen is mainly in the gas-phase due to its low solubility in water, the effective diffusion coefficient of oxygen within the CDL is [2]

$$D^e_{O_2,E} = \varepsilon_E^{1.5}(1-q_W)^{1.5}D_{O_2,E} \quad (45)$$

where the effective diffusion coefficient of oxygen $D_{O_2,E}$ in the multicomponent (N_2, H_2O, CO_2) gas-mixture may be evaluated from binary diffusion coefficients as described in [2], and q_W is the volume fraction of water in the gas pore space in the CDL, assumed as 0.5 here [2].

Similarly, the effective diffusion coefficient of methanol in the anode gas-diffusion layer (layer D) may be estimated from the relation $D^e_{Me,D} = \varepsilon_D^{1.5}(1-q_{CO_2})^{1.5}D_{Me,W}$ [13], where q_{CO_2} represents the volume fraction of the ADL pores that are occupied by CO_2 bubbles, which would be a function of current density as well as methanol feed flow rate [39]. However, unlike the case of oxygen transport in the CDL, the transport of methanol in the ADL occurs to significant level in the gas-phase as well [17] because of its high concentration as well diffusivity in the gas phase. Thus a better estimate of methanol effective diffusion coefficient in ADL would include its transport in both phases, i.e., $D^e_{Me,D} = \varepsilon_D^{1.5}\left\{(1-q_{CO_2})^{1.5}D_{Me,W} + (q_{CO_2})^{1.5}\kappa_{Me,CO_2}D_{Me,CO_2}\right\}$, where κ_{Me,CO_2} is the liquid/gas partition coefficient, which varies with temperature as well as with methanol concentration [13], and D_{Me,CO_2} is the gas-phase diffusion coefficient of methanol. Additionally, since the variation of q_{CO_2} with current density i and with temperature is not well characterized, for simplicity, we use instead the following empirical expression for the effective diffusivity, fitted to the limiting current density data of Chiu et al. [20]

$$D^e_{Me,D} = 9.75\times10^{-1}\,\exp\left(-\frac{30,975}{RT}\right) \quad (46)$$

which is the second main fitted parameter in our model.

The effective diffusion coefficient of methanol in the PEM is assumed to be similarly given by

$$D^e_{Me,B} = \varepsilon_B^{1.5}D_{Me,W} \quad (47)$$

where the methanol–water diffusion coefficient, $D_{Me,W}$, is given in Eq. (44). This provides an activation energy for the effective methanol diffusion in the PEM that is consistent with the experiments of Ren et al. [40].

In this, the volume fraction of water in the PEM ε_B depends upon λ, the number of water molecules sorbed by the electrolyte layer per acid site, i.e. [2],

$$\varepsilon_B = \frac{\lambda}{\lambda + r} \quad (48)$$

where $r = \bar{V}_B/\bar{V}_W = 537/18 \approx 30$, is the ratio of membrane partial molar volume of polymer electrolyte to that of water.

Finally, the effective oxygen diffusion coefficient in PEM in Eq. (33) is estimated from

$$D^e_{O_2,B} = \varepsilon_B^{1.5} D_{O_2,W} \tag{49}$$

where $D_{O_2,W}$ is the molecular diffusion coefficient of oxygen in liquid water.

There are few good estimates available in the literature of the mass transfer coefficient k_i in the bulk (Eq. (8)) for the electrode chambers in a DMFC. The situation is complex because of two-phase flow in the flow channels of both the electrodes. For instance at the anode, the mass transfer coefficient depends upon the hydrodynamics in the channel as well as the generation of CO_2 bubbles at the GDL surface, the extent of which depends upon the current density, i [13]. The enhanced convection by the bubbles would increase k_{Me}. On the other hand, these bubbles also reduce the effective area for liquid-phase mass transfer from the bulk to the GDL. In fact, Xu et al. [12] found little effect of current density on the mass transfer coefficient.

In the absence of better information, for now we simply adopt the following correlation for bulk-phase mass transfer coefficient under laminar flow in a square cross-section channeled monoliths of side d and length L [41]

$$\mathrm{Sh} = \frac{k_i d}{D_i} = 2.696\left(1 + 0.139\ \mathrm{Re}\,\mathrm{Sc}\frac{d}{L}\right)^{0.81} \tag{50}$$

Such relations are sometimes written in terms of Peclet number, $\mathrm{Pe} \equiv \mathrm{Re}\,\mathrm{Sc} = vd/D_i$. Further, we can write the velocity in terms of the volumetric flow rate in electrode chamber, $v = \dot{V}_\rho/(nd^2)$, where n is the number of parallel channels in the flow field, e.g., $n = 1$ for a single serpentine channel. Thus, the mass transfer coefficient becomes

$$k_i = 2.696\frac{D_i}{d}\left(1 + 0.139\frac{d^2/\tau_i}{D_i}\right)^{0.81} \tag{51}$$

where τ_i is the mean residence time of species i in the electrode chamber, and the volume of the electrode chamber = nd^2L, i.e., $\tau_i = \dot{V}_\rho/nd^2L$. Consequently, the second term in the parentheses may be construed as a ratio of hydrodynamic dispersion to molecular diffusion. This relation could be assumed to provide approximate mass transfer coefficient values for both the methanol feed (vapor or liquid) as well as for the cathode air feed.

For a passive DMFC, thus, since $\tau \to \infty$, the mass transfer coefficient, $k_i = 2.696(D_i/d)$. Further, the dimension d over which diffusion occurs under quiescent conditions can be large in a passive DMFC, so that k_i could be quite small and, hence, bulk phase diffusion resistance could be significant. In fact, the key difference between active and passive DMFCs is the much higher mass transfer coefficient for methanol as well as for oxygen in active DMFCs.

At slow flow rates, furthermore, the average concentrations of methanol and oxygen in the bulk in electrode chambers are lower than the feed concentrations due to consumption at the electrodes. In the above, in fact, we have assumed that the bulk concentrations of methanol and oxygen in the respective electrode chambers are known. However, what is known are the inlet feed concentrations. The actual average bulk concentrations in the electrode chambers may for simplicity be taken as the mean of the inlet and outlet concentrations [12], i.e.,

$$c_{i,b} = \frac{c_{i,\mathrm{in}} + c_{i,\mathrm{out}}}{2} \tag{52}$$

where the inlet and outlet concentrations are interrelated via a mass balance on the electrode chamber considered as a well-mixed, i.e.,

$$\dot{V}_\rho(c_{i,\mathrm{in}} - c_{i,\mathrm{out}}) = AN_{i,z} \tag{53}$$

where A is the MEA geometric area. Combining the above two equations and relating the species fluxes to corresponding current densities (Eq. (6)) provides for the anode [12]

$$c_{\mathrm{Me},b} = c_{\mathrm{Me,in}} - \frac{A(i + i_{X,\mathrm{Me}})}{12F\dot{V}_A} \tag{54}$$

while for the cathode

$$c_{O_2,b} = c_{O_2,\mathrm{in}} - \frac{Ai}{8F\dot{V}_C} \tag{55}$$

where the O_2 concentration must be corrected for the presence of water vapor as well (Table 1).

Finally, the Ohmic losses through the PEM are, of course, proportional to its thickness and membrane conductivity (Eq. (36)). Although more complex forms are available in literature for membrane conductivity [42], we assume the simpler expression of Thampan et al. [38]

$$\sigma_B = (\varepsilon_B - \varepsilon_{B,0})^{1.5}\left(\frac{349.8}{1+\delta}\right)\exp\left\{-\frac{E_\mu}{R}\left(\frac{1}{T} - \frac{1}{298}\right)\right\}\left(\frac{1}{18\lambda}\right)\beta \tag{56}$$

where the parameter δ varies between 0.6 and 5.5 [2,38]. In the following $\delta = 3.5$ was chosen as it agrees well with the conductivity data of Ren et al. [40] in DMFC.

The degree of dissociation of acid sites, or β, in the above, is

$$\beta = \frac{(\lambda+1) - \sqrt{(\lambda+1)^2 - 4\lambda(1 - 1/K_a)}}{2(1 - 1/K_a)} \tag{57}$$

where λ is the number of water molecules sorbed by the electrolyte layer per acid site, and the dissociation equilibrium constant for acid sites is

$$K_a = 6.2\exp\left[\frac{-52,300}{R}\left(\frac{1}{T} - \frac{1}{298}\right)\right] \tag{58}$$

In Eq. (56), further, $\varepsilon_{B,0}$ is the percolation threshold, roughly corresponding to $\lambda_0 = 1.8$. Assuming a liquid feed, we assumed the membrane to be saturated, so that $\lambda = 20$ [40].

The model parameters discussed above are summarized in Table 1.

3. Results and discussion

To check if our model as developed above with mostly a priori parameters is a good representation of the DMFC performance, its predictions are compared next with literature data. A stumbling block in such a comparison is, of course, finding a comprehensive and consistent set of data, because of the wide variability of DMFC performance reported in the literature. Chiu et al. [4,20] have recently reported such a set of data, which they kindly provided to us in tabular form, and is used below in our comparison. The general experimental conditions of Chiu et al. [4,20] are summarized in Table 2.

3.1. DMFC polarization and power density

Two of the variables that most profoundly affect DMFC performance are: (1) the feed methanol concentration, and (2) the operating temperature.

The effect of methanol feed concentration on the DMFC performance is shown in Fig. 2 along with the data of Chiu et al. [20], for fuel concentrations varying from 0.75 M to 1.5 M and air at the cathode, and at a constant operating temperature of 313 K. Fig. 2(a) shows the polarization plot (Eq. (36)), while the corresponding power density (Eq. (37)) versus current density is shown in Fig. 2(b). It can be seen that the model, with the set of parameters listed in

Table 1
DMFC model parameters.

Parameter	Value	Units	Reference/comment
ΔG°	-702.7	kJ K^{-1} mol^{-1}	Standard Gibbs free energy change
ΔH°	-726.8	kJ K^{-1} mol^{-1}	Standard enthalpy change
V_0^o	$-\Delta G^{\circ}/6F = 1.214$	V	Standard thermodynamic potential
V_{max}^o	$-\Delta H^{\circ}/6F = 1.255$	V	Standard maximum potential
ρ_{Pt}	21.45	g cm^{-3}	Platinum density
ρ_{Ru}	12.3	g cm^{-3}	Ruthenium density
$d_{M,A}$, $d_{M,C}$	2.7	nm	Typical for C supported Pt [33]
φ_I	0.75	–	[2]
$i^*_{A,0,ref}$	2.0×10^{-8}	A cm^{-2}	Fitted (the intrinsic exchange current not available in literature)
$i^*_{C,0,ref}$	1.0×10^{-10}	A cm^{-2}	[22]
$c_{Me,ref}$	1.0×10^{-3}	mol cm^{-3}	Standard
c_W	55.5×10^{-3}	mol cm^{-3}	Dilute methanol solutions
T_{ref}	298	K	Standard
$p_{O_2,ref}$	1	atm	Standard
$\dot{\alpha}_A$	1/2	–	Typical for elementary RDS
$\dot{\nu}_{A,e^-}$	+1	–	Agrees with Tafel slope of Gojkovic et al. [33]
$\dot{\alpha}_C$	1/2	–	Typical for elementary RDS
$\dot{\nu}_{C,e^-}$	-2	K	[22]
ν_{A,e^-}	+6	–	Stoichiometric coefficient of electrons in MOR
$\nu_{A,Me}$	-1	–	Stoichiometric coefficient of methanol in MOR
E_{A,Φ_0}	65	kJ mol^{-1}	[34]
E_{C,Φ_0}	67	kJ mol^{-1}	[2]
K_{Me}	$1.5 \times 10^{-8} \exp\left(\frac{130{,}000\,\text{J mol}^{-1}}{RT}\right)$		Estimated as CO adsorption equilibrium constant on Pt
L_B	178×10^{-4}	cm	Nafion® 117 thickness
L_D	260×10^{-4}	cm	[22]
L_E	260×10^{-4}	cm	[22]
ε_D, ε_E	0.65	–	Typical ADL/CDL porosity
κ_{O_2}	0.144	–	[2]
$\kappa_{Me,D}$	1.0	–	Assumed
$\kappa_{Me,B}$	0.4	–	[40]
ξ	2.9	–	[28]
E_μ	14	kJ mol^{-1}	Water viscosity activation energy
λ	20	–	[40]
δ	3.5	–	Fitted to conductivity data of Ren et al. [40]
q_W	0.5	–	Volume fraction of water in CDL pore s
$D_{Me,W}$	$2.1 \times 10^{-5} \exp\left\{-\frac{20{,}460}{R}\left(\frac{1}{T}-\frac{1}{313}\right)\right\}$	cm^2 s^{-1}	[37]
$D^e_{Me,D}$	$9.75 \times 10^{-1} \exp\left(-\frac{30{,}975}{RT}\right)$	cm^2 s^{-1}	Fitted diffusion coefficient in ADL
$D_{O_2,W}$	$7.4 \times 10^{-8} \frac{T(40.68)}{\mu(25.6^{0.6})}^{0.5}$	cm^2 s^{-1}	Oxygen diffusion coefficient in liquid water
$D_{O_2,E}$	$0.357 \times \left(\frac{T}{352}\right)^{1.823}$	cm^2 s^{-1}	Gas-phase oxygen diffusion coefficient
p_W	$\exp\left(11.676-\frac{3816.44}{T-46.13}\right)$	atm	Water vapor pressure in cathode
r	$\bar{V}_B/\bar{V}_W = 537/18$	–	[2]
R_I	0	Ω cm^2	MEA interfacial resistance

Table 1, fits the data very well throughout the voltage-current density range investigated. In other words, the model appears to be robust.

Although not readily discerned because of the scale in Fig. 2(a), the OCV as well as the cell potential V at low current densities i is actually higher for lower methanol feed concentrations, because of the lower polarization of the anode, as well as lower methanol crossover and the resultant lower polarization of the cathode. However, at higher current densities (e.g., >50 mA cm^{-2} in Fig. 2), the trend reverses, with higher cell potentials resulting at a given

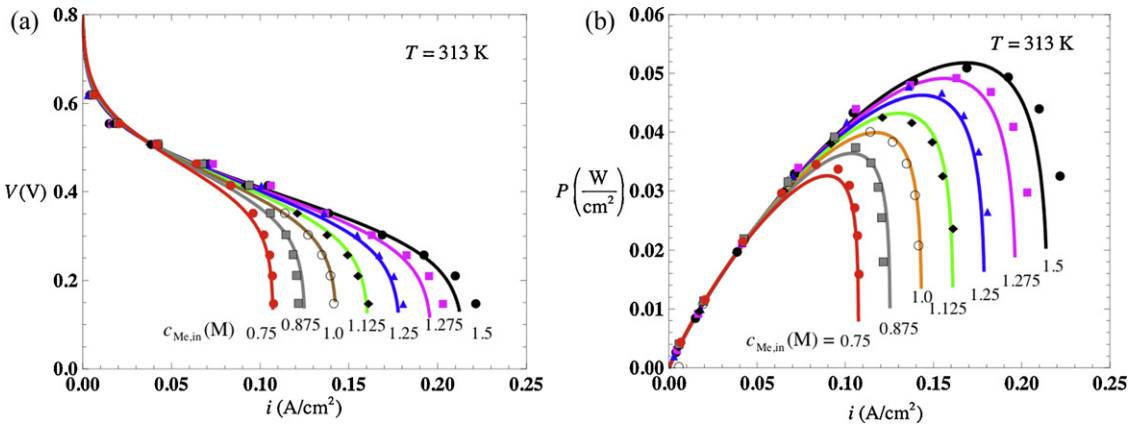

Fig. 2. Comparison of theoretical predictions with experiments of Chiu et al. [20] for (a) polarization plots and (b) power density versus current density of a DMFC operating at 313 K with air at the cathode and different methanol feed concentrations in the range of 0.75 M to 1.5 M. Table 2 provides the other experimental conditions.

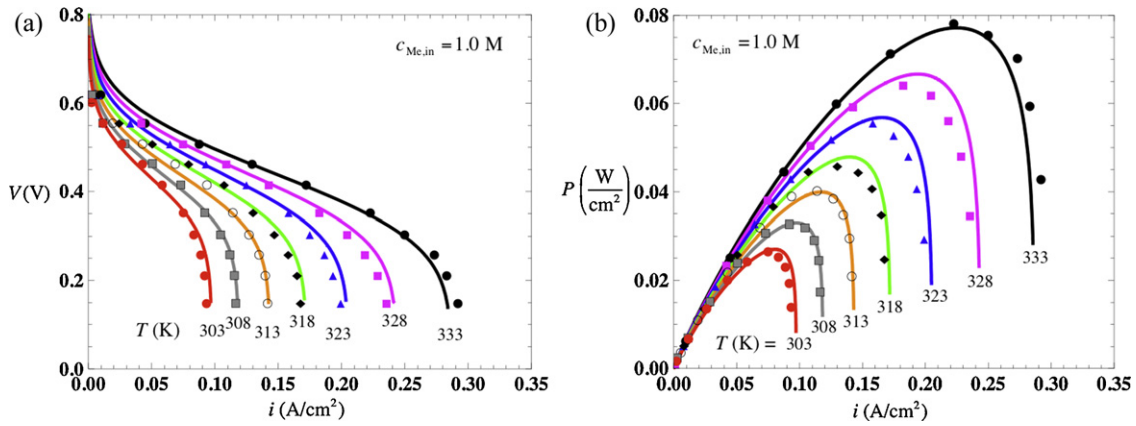

Fig. 3. Comparison of theoretical predictions with experiments of Chiu et al. [20] for (a) polarization plots and (b) power density versus current density of a DMFC operating with 1 M methanol feed and air at the cathode at different temperatures from 303 to 333 K. Table 2 provides the other experimental conditions.

current density for the higher methanol feed concentrations. This is by virtue of higher diffusion limitations in the ADL, i.e., lower limiting current densities, $i_{A,L}$, at the lower methanol feed concentrations. Likewise in Fig. 2(b), the curves are bunched together at lower current densities but then diverge at higher current densities, when the higher methanol feed concentrations can produce more power. The power density then peaks before declining as the DMFC performance becomes dominated by diffusion limitations in the GDL at higher current densities. Thus, there is, an optimum power density for a given methanol feed concentration.

The effect of temperature on DMFC performance is illustrated in Fig. 3, where polarization plots are provided in Fig. 3(a) at different temperatures for the DMFC operating with air at the cathode and at a methanol feed concentration of 1.0 M, while power density is plotted as a function of current density in Fig. 3(b). Although the plots are qualitatively similar to those in Fig. 2, there are important differences. First of all, there is a steady increase with temperature in cell voltage as well as power density for a given current density throughout the range of current densities. This is because the higher temperatures significantly enhance electrode kinetics, as well as transport processes, both proton transport in the PEM [5], as well as diffusion across the GDLs. The increase in cell voltage and power density with temperature at lower current densities is a clear indication of improving electrode kinetics at both the anode and the cathode. The reduction of slope in the polarization plot in Fig. 3(a) at the intermediate current densities indicates a reduction in the Ohmic resistance of the PEM. Finally, the increase in limiting current densities with temperature is a clear indication of improvement in the transport across the GDL. In short, the higher the operating temperature in the range investigated, the better, provided it is not so high that the cathode is asphyxiated by the rapidly rising vapor pressure of water.

Further, methanol crossover escalates with temperature as well, so that we might expect that there is an optimum temperature for a given methanol feed concentration.

The maximum cell power density, P_{max}, as a function of temperature and feed composition, as shown in Figs. 2(b) and 3(b) can, in fact, be determined analytically by taking the derivative of the power density (Eq. (37)) with respect to current density, and setting it equal to zero to determine the corresponding optimum current density, which, when used back in Eq. (37), provides P_{max}. Such information is crucial for developing control strategies for a DMFC power plant, e.g., for real-time control of DMFC.

3.2. Crossover and its impact on electrode overpotentials and OCV

Methanol crossover is the central issue in DMFCs that is known to not only represent fuel loss but also increase the cathode overpotential. To investigate methanol crossover further, Fig. 4 provides a comparison of the experimental results of Chiu et al. with the predicted methanol crossover current density (Eq. (27)) as a function of the fuel cell current density at different operating temperatures for a 1.0 M methanol feed and using the set of parameters in Table 1. It

Table 2
Experimental conditions of Chiu et al. [4,20].

Item	Description
Commercial MEAs	35 mm × 35 mm duPont, with Nafion® 117
Anode catalyst	40 wt% Pt–Ru/C, Pt/Ru wt ratio 1:1
Cathode catalyst	40 wt% Pt/C
Pt loading	2 mg cm^{-2} at both anode and cathode
Graphite channel	Single serpentine, 1 mm wide × 1 mm deep
Anode flow rate (liquid feed), $\dot{V}_A$	5 ml min^{-1}
Cathode flow rate (Air), $\dot{V}_C$	150 ml min^{-1}
Operating temperatures, T (K)	303, 308, 313, 318, 323, 328, 333
Methanol feed concentrations, $c_{Me,in}$ (M)	0.75, 0.875, 1.0, 1.125, 1.25, 1.375, 1.5, 2.0

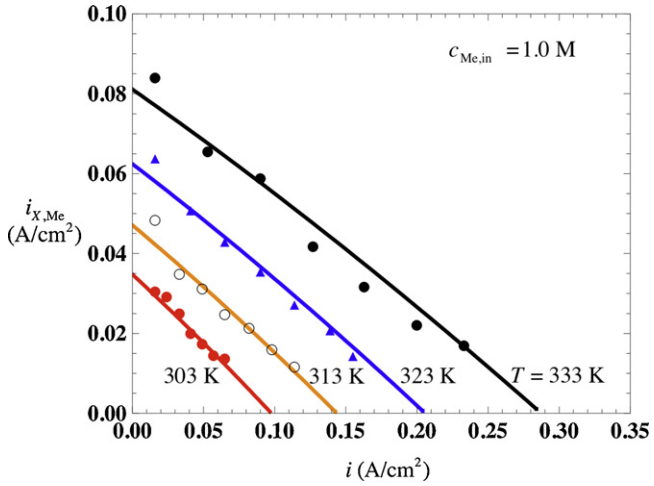

Fig. 4. Comparison of theoretical predictions with experiments of Chiu et al. for methanol crossover current density versus current density at different temperatures for a DMFC operating with1.0 M methanol feed and air at the cathode. Table 2 provides the other experimental conditions.

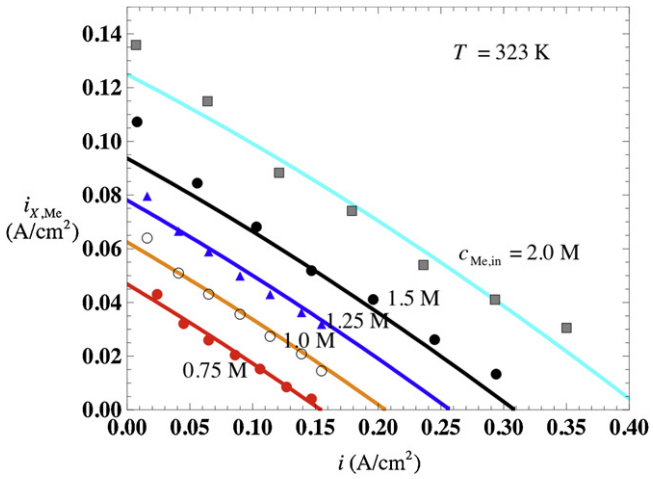

Fig. 5. Comparison of theoretical predictions with experiments of Chiu [4] for methanol crossover current density versus current density at different methanol feed concentrations for a DMFC operating at 323 K with air at the cathode. Table 2 provides the other experimental conditions.

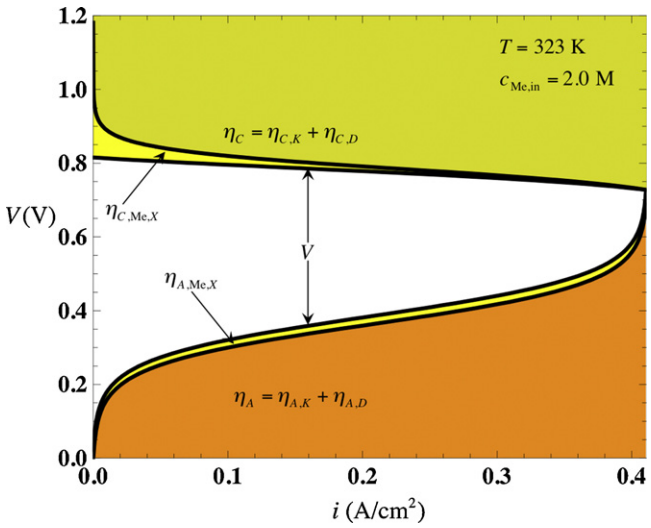

Fig. 6. Predicted anode and cathode overpotentials, including contributions of methanol crossover, of a DMFC operating at 50 °C with a 2 M methanol feed and air at the cathode.

is noteworthy that crossover current density is of the same order as fuel cell current density even at this low methanol feed concentration. Methanol crossover is, of course, contributed by both diffusion, dependent on methanol concentration, and electro-osmotic drag, dependent on current density.

At zero current density, or under OCV conditions, the methanol crossover current density is the highest, corresponding to Eq. (28), and accounts for the significant drop of OCV below the thermodynamic voltage of DMFC. It is seen in Fig. 4 that crossover current density at OCV increases sharply with temperature. As the DMFC current density increases, however, more of the methanol is consumed within the ACL and, thus, less is available for diffusion across the PEM, so that the crossover current density declines (Fig. 4), eventually approaching zero as the fuel cell current density approaches the limiting current density. Nonetheless, there is a sharp increase in the methanol crossover at all current densities with temperature.

There is also a qualitatively similar relationship between methanol crossover current density versus fuel cell current density for varying methanol feed concentrations at a given operating temperature, as shown in Fig. 5. It is seen, once again, that the model does a nice job of simulating the experimental data of Chiu [4] without any additional fitting.

Since the model, thus, appears robust, let us use it to further explore the effect of crossover on electrode overpotential as well as on OCV. Thus, the model is used, along with the parameters in Table 1, to theoretically predict the cathode as well as anode polarization as shown in Fig. 6, for the experimental conditions of Chiu et al. [20] (Table 2), and for an assumed methanol feed concentration of 2 M and an operating temperature of 323 K.

The upper curve in Fig. 6 represents the cathode polarization because of kinetic and diffusion limitations of ORR, $\eta_C = \eta_{C,K} + \eta_{C,D}$, while the yellow sliver below it is the contribution of methanol crossover to the cathode overpotential, $\eta_{C,Me,X}$. Thus, the upper shaded area represents cathode power consumption for a H_2–O_2 fuel cell, to which when is added the yellow area representing the polarization and corresponding power consumption because of methanol crossover, the total cathode polarization loss due to a DMFC cathode results. It is seen that while the ORR sluggishness is the dominant cause of cathode polarization, the contribution of the methanol crossover is significant especially at the lower current densities, in accord with experimental observations [43]. Further, when the ORR is diffusion limited at high current densities, although not shown in Fig. 6, again the contribution of methanol crossover to cathode overpotential can become significant, as it reduces the effective cathode limiting current density because of oxygen consumption by the methanol that has crossed over.

The lower region in Fig. 6 represents the anode polarization losses. Again the yellow sliver in the figure represents the effect of methanol crossover. Thus, there is not an insignificant *anode* polarization loss due to methanol crossover. The orange region below it represents kinetic and diffusion limitations of the MOR, $\eta_A = \eta_{A,K} + \eta_{A,D}$, determined by setting the term representing the crossover current density of methanol equal to zero in the anode overpotential, Eq. (30).

It is, thus, noteworthy that the methanol crossover is predicted to increases the polarization of the *anode* as well, in addition, of course, to that of the cathode, something that has not apparently been discussed in the literature so far. The limiting current density of the cell in the example in Fig. 6 is determined by $i_{A,L}$, which in turn is determined mainly by the methanol feed concentration [44]. Finally, the colorless region between the cathode and the anode polarization regions in Fig. 6 represents the useful electric power produced in the DMFC, the vertical distance between the two overpotential curves being the observed voltage, *V*.

Another potential issue affecting DMFC performance that has not so far been discussed in the literature is the anode polarization because of *oxygen* crossover, illustrated in Fig. 7. Although in a well-assembled, air-fed DMFC, the O_2 crossover current is small ($<1\ mA\ cm^{-2}$), it could be non-negligible when the anode chamber is open to air, as in a passive DMFC to vent CO_2, or when account is taken of the O_2 dissolved in an air-equilibrated methanol feed. As Fig. 7 shows, ingress of O_2 at the anode can not only substantially impact the OCV, but also the entire polarization plot as well as the diffusion restricted anode limiting current density.

According to Eq. (38), the thermodynamic voltage in a DMFC under typical operating conditions is about 1.18 V. However, the actual OCV is only about half as much [20], depending upon the operating temperature and the methanol feed concentration. This is primarily because of the combined effect of the methanol crossover, and the sluggish ORR in oxidizing the methanol at the cathode (Fig. 6). As the methanol concentration increases, methanol crossover becomes more significant (Fig. 5), reducing the OCV even further.

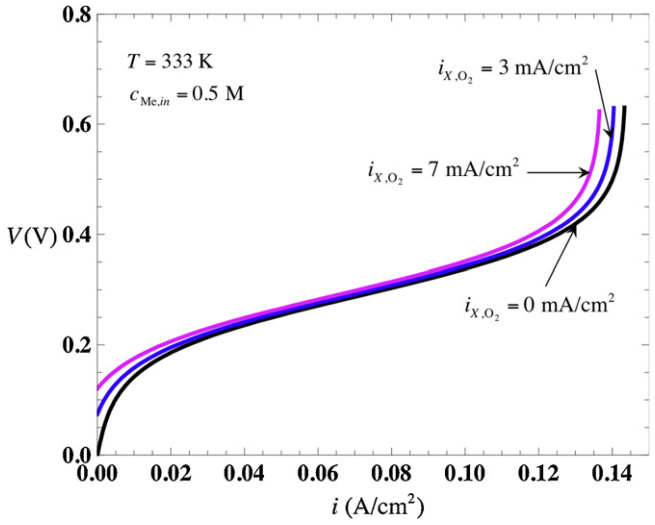

Fig. 7. The predicted effect of oxygen crossover current density on anode overpotential.

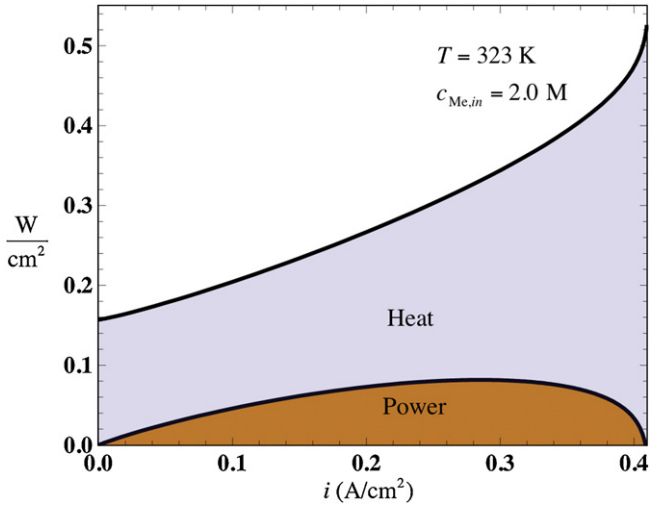

Fig. 9. A comparison of predicted heat flux dissipation and electric power density produced versus current density in a DMFC operating at 323 K with a 2 M methanol feed and air at the cathode.

The OCV can, in fact, be predicted simply by setting $i = 0$ in the DMFC polarization expression, Eq. (38), resulting in

$$\mathrm{OCV} = V_0 - \frac{RT}{\dot{\alpha}_A \dot{\nu}_{A,e^-} F}\sinh^{-1}\left\{\frac{1}{2}\left(\frac{i_{X,O_2}/i_{A,0}}{1 - i_{X,O_2}/i_{A,L}}\right)\left(1 + \frac{i_{X,Me,L}}{i_{A,L}}\right)\right\} + \frac{RT}{\dot{\alpha}_C \dot{\nu}_{C,e^-} F}\sinh^{-1}\left\{\frac{1}{2}\left(\frac{i_{X,Me,0}/i_{C,0}}{1 - i_{X,Me,0}/i_{C,L}}\right)\right\} \quad (59)$$

i.e., both oxygen and methanol crossover can affect the OCV. Thus, the OCV is plotted in Fig. 8 as a function of temperature as well as feed methanol concentration for a DMFC operating on air at the cathode. Clearly, the OCV declines monotonically with increasing methanol concentrations at all temperatures.

The dominant effect on OCV is, of course, that of the methanol crossover under zero current conditions, i.e., $i_{X,Me,0}$, as given by Eq. (28). From Eqs. (28) and (59), thus, for the case when the oxygen crossover may be neglected, the OCV may be written as

$$\mathrm{OCV} = V_0 + \frac{RT}{\dot{\alpha}_C \dot{\nu}_{C,e^-} F}\sinh^{-1}\left\{\frac{i_{X,Me,L}/2i_{C,0}}{1 + i_{X,Me,L}((1/i_{A,L}) - (1/i_{C,L}))}\right\} \quad (60)$$

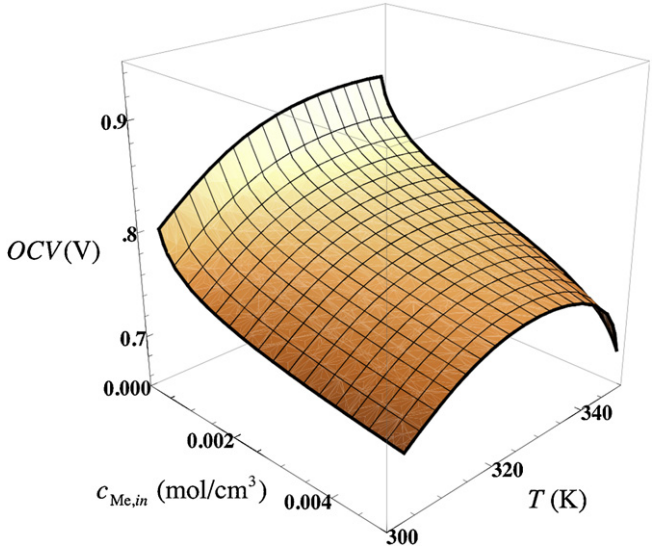

Fig. 8. Predicted OCV as a function of operating temperature (300–350 K) and feed methanol concentration (0.1–5.0 M, or 0.1×10^{-3} to 5.0×10^{-3} mol cm^{-3}) for an air fed DMFC.

While the OCV declines monotonically with concentration at a given temperature (Fig. 8), it is seen that at higher methanol feed concentrations, the OCV is not a monotonic function of temperature, although that is the case at the lower methanol concentrations. The electrode kinetics at the anode as well as the cathode improve with temperature, reducing the electrode overpotentials. On the other hand, methanol diffusion through the membrane increases with temperature, as does the crossover with temperature. Even more significantly, the vapor pressure of water increases quickly with temperature (Table 1), smothering the cathode and consequently reducing the cathodic diffusion restricted limiting current density, $i_{C,L}$.

3.3. DMFC Efficiency

The enthalpy of combustion of the fuel, ΔH, that is not converted into useful electric power (Eq. (37)) because of the various irreversibilities in the anode, cathode, and the PEM, is dissipated by the DMFC as low-grade heat [45], which must, consequently, be managed for maintaining the desired operating temperature. The heat dissipation flux (W cm^{-2} MEA) is determined from

$$q = V_{\max}(i + i_{X,Me} + i_{X,O_2}) - P \quad (61)$$

where P is given by Eq. (37), and $V_{\max} \equiv -\Delta H/(n_{e^-}F)$. For DMFC, $V^o_{\max} = 1.255$ V under *standard* conditions, while, of course, the thermodynamic potential $V^o_0 = -\Delta G/n_{e^-}F = 1.214$ V under standard conditions, i.e., the thermodynamic efficiency under standard conditions, $\varepsilon^o_0 = V^o_0/V^o_{\max} = 1.214/1.255 = 96.7\%$.

The heat flux generated versus current density is plotted in Fig. 9 for illustrative purposes for the operating conditions of Fig. 6. It is obvious that a substantial amount of heat is generated in a PDMFC, while only a relatively small fraction of the energy of the fuel is converted into electric power, much as Eccarius et al. [46] have reported. Thus, the DMFC suffers from a low efficiency, clearly because of the large electrode overpotentials coupled with methanol crossover, which reduces the current efficiency. The generated heat can, in fact, be used to raise the operating temperature of a passive DMFC [47] and, thus, improve performance, as

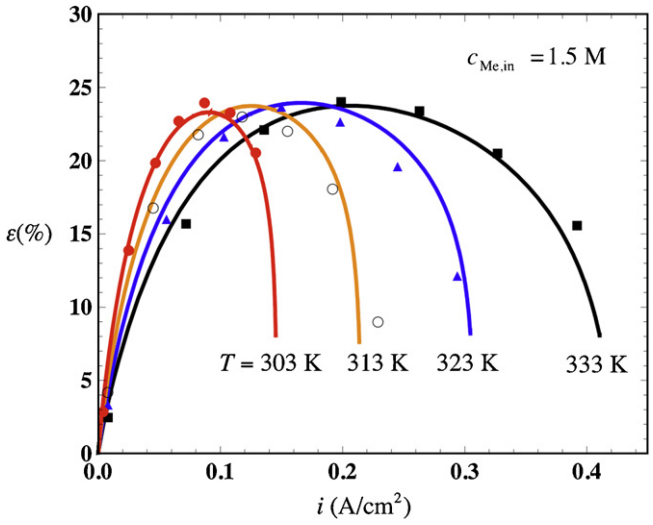

Fig. 10. Comparison of theoretical predictions of efficiency versus current density, with experimental efficiency calculated from the data of Chiu et al. [20] at different temperatures for a DMFC operating with a 1.5 M methanol feed and air at the cathode. Table 2 provides the other experimental conditions.

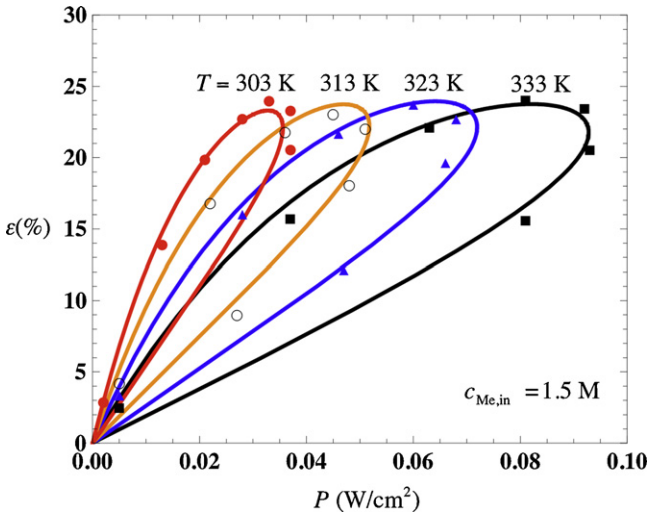

Fig. 11. Comparison of theoretically predicted petal-shaped plots of efficiency versus power density, with experimental efficiency calculated from the data of Chiu et al. [20] at different temperatures for a 1.5 M methanol feed and air at the cathode. Table 2 provides the other experimental conditions.

shown by Casalegno et al. [48]. However, as discussed above, too high a temperature also enhances methanol crossover, and further stifles the cathode because of the higher vapor pressure of water within the cathode chamber.

The overall DMFC efficiency [49,50] may be determined from a product of the thermodynamic, current, and voltage efficiencies, i.e.,

$$\varepsilon \equiv \varepsilon_0 \varepsilon_i \varepsilon_V = \left(\frac{V_0}{V_{\max}}\right)\left(\frac{i}{i + i_{X,\mathrm{Me}} + i_{X,\mathrm{O_2}}}\right)\left(\frac{V}{V_0}\right) = \frac{P}{V_{\max}(i + i_{X,\mathrm{Me}} + i_{X,\mathrm{O_2}})} \quad (62)$$

Fig. 10 shows a comparison of theoretical predictions with experimental efficiencies at different temperatures for a 1.5 M methanol feed and air on the cathode, calculated based on Eq. (62) and utilizing the experimental data of Chiu et al. [20] for power density, P, current density, i, and the crossover current density, $i_{X,\mathrm{Me}}$, while assuming that the oxygen crossover current density, $i_{X,\mathrm{O_2}} \to 0$. A similar comparison is provided in Fig. 11 for DMFC efficiency versus power density at different temperatures for a 1.5 M methanol feed and air on the cathode.

The maximum efficiency observed for the DMFC conditions investigated is around 24%, which does not appear to vary much with temperature, although the peaks becomes broader with temperature, i.e., higher efficiencies can be obtained over a broader range of operating current densities with temperature. This is useful in applications where the load can vary significantly.

The peaks in efficiencies observed in Fig. 11 as a function of power density appear even sharper in the petal-shaped plots. The reason these petal plots go through the origin is that the efficiency $\varepsilon = 0$ when $P = 0$, both under OCV conditions, when $i = 0$, as well as under limiting current density conditions, when $V = 0$. So, as one traverses from OCV to limiting current density (clockwise on the petal), the efficiency first increases, peaks, and then declines, returning back to zero. The agreement with theory is once again quite good. It is seen that there is only a narrow range of operation indicated if peak power density as well as peak efficiency are desired. Such plots and relationships can, thus, be very useful for algorithmic control of DMFCs to operate in the region of peak efficiencies and power densities, which is clearly important in portable applications.

Finally, although not discussed in this paper, the model presented here is useful in exploring design aspects of DMFCs, e.g., effect of the catalyst loading and particle size, and membrane thickness [51], etc. In general, thicker membranes perform better at lower current densities and generate higher OCV due to lower crossover, although thinner membranes exhibit better performance at higher current densities because of smaller electrolyte resistance. Of course, the model may be used for diagnostic purposes as well, e.g., a decline in OCV may be an indication of membrane degradation/thinning. The interfacial resistance in the above analysis has been assumed to be zero. While this may be valid for a well-fabricated MEA, an increase in the resistance with time might, for instance, indicate delamination of the layers, or simply a poorly fabricated MEA.

4. Conclusions

The direct methanol fuel cell is very attractive for portable and backup power, and is starting to make inroads into some of these markets, e.g., as an on-the-go forklift battery charger. However, its high cost and relatively unimpressive power density remain significant barriers. Operating DMFC under optimal power density and efficiency requires a clear understanding of how the various design and operational parameters affect its performance. We have, thus, developed a transparent *albeit* rigorous analytical model based on some key judicious but defensible assumptions. The resulting analytical expressions for crossover current density, DMFC polarization, and power density are in terms of quantities with discernable physical meaning, so that their effect on DMFC performance can be better appreciated.

The model, with mainly two fitted parameters, has been rigorously tested against an extensive and consistent data set on DMFC performance, and found to be in broad agreement. Thus, the model accurately predicts the influence of methanol crossover on OCV as well as on the overall cell performance under a variety of feed concentrations and temperatures. The fuel cell power density and efficiency under different operating can be accurately predicted as well. Consequently, the model can be used for developing control algorithms for operating under optimal conditions, e.g., by carefully controlling online the methanol feed concentration. It can also be used for diagnostics. Finally, the model should help in improved understanding of the DMFC.

Acknowledgement

We thank Prof. Yu-Jen Chiu of the Technology and Science Institute of Northern Taiwan for kindly providing in tabular form their experimental data on DMFC performance published in refs [4,20], which we have used extensively here for validating our model.

References

[1] M.P. Hogarth, T.R. Ralph, Platinum Met. Rev. 46 (2002) 146–164.
[2] T. Thampan, S. Malhotra, J. Zhang, R. Datta, Catal. Today 67 (2001) 15–32.
[3] C.-Y. Wang, Chem. Rev. 104 (2004) 4727–4766.
[4] Y.-J. Chiu, Int. J. Hydrogen Energy 35 (2010) 6418–6430.
[5] P.S. Kauranen, E. Skou, J. Munk, J. Electroanal. Chem. 404 (1996) 1–13.
[6] C.Y. Du, T.S. Zhao, W.W. Yang, Electrochim. Acta 52 (2007) 5266–5271.
[7] J.G. Liu, T.S. Zhao, R. Chen, C.W. Wong, Electrochem. Commun. 7 (2005) 288–294.
[8] B. Bae, B.K. Kho, T.-H. Lim, I.-H. Oh, S.-A. Hong, H.Y. Ha, J. Power Sources 158 (2006) 1256–1261.
[9] D. Chu, R. Jiang, Electrochim. Acta 51 (2006) 5829–5835.
[10] R. Jiang, D. Chu, J. Electrochem. Soc. 151 (2004) A69–A76.
[11] G.-B. Jung, A. Su, C.-H. Tu, F.-B. Weng, S.-H. Chan, R.-Y. Lee, S.-H. Wu, J. Fuel Cell Sci. Technol. 4 (2007) 248–254.
[12] C. Xu, Y.L. He, T.S. Zhao, R. Chen, Q. Ye, J. Electrochem. Soc. 153 (2006) A1358–A1364.
[13] K. Sundmacher, K. Scott, Chem. Eng. Sci. 54 (1999) 2927–2936.
[14] B.L. Garcia, V.A. Sethuraman, J.W. Weidner, R.E. White, J. Fuel Cell Sci. Technol. 1 (2004) 43–48.
[15] A.A. Kulikovsky, Electrochem. Commun. 4 (2002) 939–946.
[16] J.P. Meyers, J. Newman, J. Electrochem. Soc. 149 (2002) A718–A728.
[17] Z.H. Wang, C.Y. Wang, J. Electrochem. Soc. 150 (2003) A508–A519.
[18] R. Chen, T.S. Zhao, J. Power Sources 152 (2005) 122–130.
[19] J. Rice, A. Faghri, Int. J. Heat Mass Transfer 51 (2008) 948–959.
[20] Y.-J. Chiu, T.L. Yu, Y.-C. Chung, J. Power Sources 196 (2011) 5053–5063.
[21] H. Dohle, K. Wippermann, J. Power Sources 135 (2004) 152–164.
[22] S.A. Vilekar, R. Datta, J. Power Sources 195 (2010) 2241–2247.
[23] S. Ma, E. Skou, Solid State Ionics 178 (2007) 615–619.
[24] Z. Jusys, R.J. Behm, Electrochim. Acta 49 (2004) 3891–3900.
[25] S.A. Vilekar, I.I. Fishtik, R. Datta, J. Electrochem. Soc. 157 (2010) B1040–B1050.
[26] R. Datta, S.A. Vilekar, Chem. Eng. Sci. 65 (2010) 5976–5989.
[27] P.S. Kauranen, E. Skou, J. Appl. Electrochem. 26 (1996) 909–917.
[28] X. Ren, S. Gottesfeld, J. Electrochem. Soc. 148 (2001) A87–A93.
[29] S.C.S. Lai, N.P. Lebedeva, T.H.M. Housmans, M.T.M. Koper, Top. Catal. 46 (2007) 320–333.
[30] J.X. Wang, J. Zhang, R.R. Adzic, J. Phys. Chem. A (2007) 12702–12710.
[31] M.R. Shivhare, C.L. Jackson, K. Scott, E.B. Martin, J. Power Sources 173 (2007) 140–248.
[32] S.A. Vilekar, I. Fishtik, R. Datta, J. Catal. 252 (2007) 258–270.
[33] Lj. Gojkovic, T.R. Vidakovic, D.R. Durovic, Electrochim. Acta 48 (2003) 3607–3614.
[34] G. Méli, J.-M. Léger, C. Lamy, R. Durand, J. Appl. Electrochem. 23 (1993) 197–202.
[35] H.A. Gasteiger, N. Markovic, P.N. Ross Jr., E.J. Cairns, J. Electrochem. Soc. 141 (1993) 1795–1803.
[36] S. Desai, M. Neurock, Electrochim. Acta 48 (2003) 3759–3773.
[37] Y.E. Lee, S.F.Y. Li, J. Chem. Eng. Data 36 (1991) 240–243.
[38] T. Thampan, S. Malhotra, H. Tang, R. Datta, J. Electrochem. Soc. 147 (2000) 3242–3250.
[39] S. Arisetty, S.G. Advani, A.K. Prasad, Heat Mass Transfer 44 (2008) 1199–1206.
[40] X. Ren, T.E. Springer, T.A. Zawodzinski, S. Gottesfeld, J. Electrochem. Soc. (2000) 466–474.
[41] M. Uberoi, C.J. Pereira, I & EC Res. 35 (1996) 113–116.
[42] P. Choi, N.H. Jalani, R. Datta, J. Electrochem. Soc. 152 (2005) E123–E130.
[43] V.A. Paganin, E. Sitta, T. Iwasita, W. Vielstich, J. Appl. Electrochem. 35 (2005) 1239–1243.
[44] T. Vidakovic, M. Christov, K. Sundmacher, J. Electroanal. Chem. 580 (2005) 105–121.
[45] S.K. Kamarudin, F. Achmad, W.R.W. Daud, Int. J. Hydrogen Energy 34 (2009) 6902–6916.
[46] S. Eccarius, F. Krause, K. Beard, C. Agert, J. Power Sources 182 (2008) 565–579.
[47] B. Xiao, H. Bahrami, A. Faghri, J. Power Sources 195 (2010) 2248–2259.
[48] A. Casalegno, P. Grassini, R. Marchesi, Appl. Therm. Eng. 27 (2007) 748–754.
[49] R. O'Hayre, S.W. Cha, W. Colella, F.B. Prinz, Fuel Cell Fundamentals, John Wiley & Sons, New Jersey, 2006.
[50] S.H. Seo, C.S. Lee, Appl. Energy 87 (2010) 2597–2604.
[51] J.G. Liu, T.S. Zhao, Z.X. Liang, R. Chen, J. Power Sources 153 (2006) 61–67.